Heavy ion collisions: puzzles and hopes

Jean-Paul Blaizot

IPhT-CEA Saclay, 91191 Gif-sur-Yvette cedex, France

DOI: http://dx.doi.org/10.3204/DESY-PROC-2010-01/28

This talk is a brief summary of some theoretical issues in the field of hot and dense QCD matter and ultra-relativistic heavy ion collisions.

1 Introduction

The study of ultra-relativistic heavy ion collisions offers the possibility to address several fundamental questions about the state of matter at very high temperature and density, or about the structure of the wave-function of a nucleus at asymptotically high energy. The reason why this second issue appears in the context of heavy ion collisions is related to the need to understand how dense and hot matter is produced there, and this requires a good knowledge of the nuclear wave-functions, and in particular of their small x partons. This feature contributes to bring together the fields of "small x" physics and that of ultra-relativistic heavy ions, with the common goal of studying QCD in regimes of large parton densities.

The extreme situations alluded to the above are believed to bring simplicity to the theoretical description of the systems under study. The naive picture of the quark-gluon plasma belongs to such asymptotic idealizations: as a natural consequence of the QCD asymptotic freedom, one expects indeed hadronic matter to turn at high temperature and density into a gas of quarks and gluons whose free motion is only weakly perturbed by their interactions. However, the data that have been collected over the last decade at RHIC [1] suggest that the temperature reached in present nuclear collisions is presumably not high enough, or is attained for too short a period of time to lead to such an idealized state of matter. The data rather provide evidence that the quark-gluon plasma produced in RHIC collisions is strongly coupled, and behaves as a "perfect liquid" rather than an ideal gas.

The origin of the strongly coupled character of the quark-gluon plasma is one of the several "puzzles" that RHIC is leaving us with, one that I shall briefly address in this talk. The "hopes" mentioned in the title of the talk reflect of course the exciting perspectives opened by the LHC: many of the questions left open by RHIC will be, hopefully, clarified there, and, perhaps, the high energies available at the LHC will be sufficient to produce the ideal quark-gluon plasma.

2 The QCD phase diagram

The study of dense and hot matter is not directly concerned with the properties of individual, elementary, particles, as is traditionally the case in particle physics. Rather, one is interested in the behavior of collections of large numbers of such particles, and in the various "phases" in which such systems may exist. Properties of QCD matter (matter made of quarks and gluons)

can be studied as a function of various control parameters, the most relevant ones (because they are directly accessible experimentally) being the temperature and the baryonic chemical potential.

Simple considerations allow us to draw the main features of the phase diagram. A basic property of QCD is the confinement of color charges: at low density and temperature quarks and gluons combine into color singlet hadrons that make up hadronic or nuclear matter. When the density, or the temperature, become high enough quarks and gluons start to play a dominant role in the thermodynamics, leading possibly to a transition to a phase of matter where color is "deconfined". Chiral symmetry (an exact symmetry of QCD when quark masses vanish) is spontaneously broken in the hadronic world, but is expected to be restored at high temperature and density. At large baryon chemical potentials, a rich structure appears in the phase diagram, yet largely unexplored (for a recent review see e.g. [3, 4]). Among the salient features, let us mention the emergence of color supraconductivity at large density, the possible existence of a critical point, as well a a possible new phase of "quarkyonic" matter whose existence has been conjectured recently on the basis of large N_c arguments [5].

3 The ideal baryonless quark-gluon plasma

There are at least two good reasons to focus on the case of baryon-free matter: i) the baryonless quark-gluon plasma is that for which we can do the most elaborate calculations from first principles, using in particular lattice gauge theory; ii) this is likely the state of matter created in the early stages of nucleus-nucleus collisions in the central rapidity region.

The QCD asymptotic freedom

QCD is "asymptotically free", which means that the interactions between quarks and gluons become weak when the typical energy scale (Q) involved is large compared to Λ_{QCD}. The strong coupling constant "runs", according to the (one-loop) formula $\alpha_s = \frac{g^2}{4\pi} \approx 1/\ln(Q/\Lambda_{QCD})$. Because the natural scale in thermodynamical functions is $Q \simeq 2\pi T$, this formula leads us to expect that matter becomes simple when $T \gg \Lambda_{QCD}$: it turns into an ideal gas of quarks and gluons. Weak coupling calculations (based on resummed QCD perturbation theory), that reproduce lattice results for temperatures greater than 2.5 to 3 T_c [6], suggest that the dominant effect of interactions is to turn (massless) quarks and gluons into weakly interacting (massive) quasiparticles. The thermodynamic functions such as the pressure, the entropy density or the energy density, all go to their corresponding Stefan-Boltzmann values at high temperature. This is confirmed by new lattice calculations that can probe arbitrarily large temperatures, and which demonstrate the approach to the Stefan-Boltzmann limit in a convincing way, in good agreement with weak coupling calculations [7].

The cross-over between hadronic matter and the quark-gluon plasma

Most recent lattice calculations indicate that the transition from the hadronic world to the quark gluon plasma is not a phase transition proper, but a smooth crossover [8], extending over a range of temperatures of the order of 20 to 30 MeV. This implies in particular that there is no unique way to define the "transition temperature" T_c: it depends somewhat on how it is measured. Thus one may define the "chiral transition temperature" as the location of the

peak in the chiral susceptibility, and this may differ from the "deconfinement temperature" measured for instance by the inflexion point in the Polyakov loop expectation value (note that this terminology is not meant to imply the existence of "two" transitions !). Independently of this basic ambiguity, some discrepancy remains as to the precise temperature location of the transition region [9, 10], but this is being resolved [11].

Between T_c and $\sim 3T_c$, there is a significant deviation between the energy density ϵ, and $3P$, where P is the pressure. The quantity $\epsilon - 3P$, which equals the trace of the energy momentum tensor, would vanish (for massless quarks) if it were not for the fact that the QCD coupling runs and depends on the temperature. The finite value of $\epsilon - 3P$ is related to the so-called QCD scale anomaly. It is appreciable only for $T \lesssim 3T_c$, and below T_c it receives contributions from the massive hadrons. This region between T_c and $3T_c$, is a difficult region where the physics is not well understood, but for which much theoretical effort is needed, since this is presumably the region where the quark-gluon plasma produced at RHIC spends most of its existence. Among the important open questions, one concerns the fate, in this region, of the quasiparticles that dominate the thermodynamics at higher temperature.

4 From the "ideal gas" to the "perfect liquid"

We shall examine now some of the RHIC results (see the talk by R. Bellwied for a more exhaustive presentation [2]), focusing on a few which suggest in the most convincing way that matter produced at RHIC is strongly interacting.

Matter is opaque to the propagation of jets

This is seen in several ways. First by looking at the correlations among the produced particles, and observing that in most central Au-Au collisions, the usual companion of a jet, expected at 180 degrees from the trigger jet, is absent [12]. Another view of the same physics is obtained by studying the so-called nuclear modification factor, a ratio that summarizes the deviation from what would be obtained if the nucleus-nucleus collision was an incoherent superposition of nucleon-nucleon collisions. The attenuation which persists at fairly large transverse momentum is usually discussed in terms of the energy loss of the leading parton in the dense medium [13]. This energy loss is found to be large and difficult to account for in a perturbative scheme (see e.g. [14] for a recent discussion).

Matter flows like a fluid

If nucleus-nucleus collisions were simple superpositions of nucleon-nucleon collisions, the produced particles would have isotropic distributions, irrespective of the shape of the collision zone in the transverse plane. However, if the interactions among the produced particles are sufficiently strong to bring the system close to local equilibrium, then a collective motion emerges: strong pressure gradients are induced by the anisotropy of the initial interaction zone, leading to anisotropic momentum distributions[15]. This so-called elliptic flow has been observed at RHIC, and is a beautiful evidence of collective behavior and (at least partial) thermalization of the produced matter.

The quark-gluon plasma as a perfect fluid

The hydrodynamical calculations that are used to analyze the flow data require a short equilibration time and a relative low viscosity, i.e. a ratio of viscosity to entropy density lower than about 0.4 [16]. Such a low value points to the fact that matter is strongly interacting, since the ratio of viscosity to entropy density would be much larger in a weakly interacting system. In fact, the "measured" value is not too different from that obtained in some gauge theories that can be solved exactly at strong coupling: $\eta/s = 1/4\pi \approx 0.08$ [17], a value that has been conjectured to be a lower bound [18]. The small value of η/s obtained for the quark-gluon plasma found at RHIC is what has motivated its qualification as a "perfect liquid".

5 Is the quark-gluon plasma strongly coupled ?

The opacity of matter, the elliptic flow, and the small value of η/s are measurements that contribute to build a picture of the quark-gluon plasma as a strongly coupled system.

The ideal strongly coupled quark-gluon plasma

In fact, the RHIC data have produced a complete shift of paradigm in the field, suggesting a new ideal system that can be used as a reference system: the strongly coupled quark-gluon plasma (sQGP). This was made possible by a theoretical breakthrough that allows one to perform calculations in some strongly coupled gauge theories, using the so-called AdS/CFT correspondence, a mapping between a strongly coupled gauge theory and a weakly coupled (i.e. classical) gravity theory. This correspondence has led to the detailed calculations of many properties of strongly coupled non abelian plasmas (for a recent review see [19]). Among the successes of this approach, let us recall the exact results for the entropy density $s/s_0 = 3/4$, and for the viscosity to entropy density ratio $\eta/s = 1/4\pi$ that we have just mentioned.

A puzzling situation: weakly or strongly coupled ?

The interpretation of RHIC data in terms of a strongly coupled quark-gluon plasma leads to a somewhat puzzling situation. There is indeed no evidence that in the transition region the QCD coupling constant becomes so huge that weak coupling techniques (with appropriate resummations) are meaningless. And we know that for temperatures above $3T_c$ such calculations account well for lattice data. Besides, the description of the early stages of nucleus-nucleus collisions in terms of the color glass condensate (see below) relies heavily on weak coupling concepts.

A possible way out this paradoxical situation is to acknowledge the coexistence, within the quark-gluon plasma, of degrees of freedom with different wavelengths, and whether these degrees of freedom are weakly or strongly coupled depends crucially on their wavelengths: short wavelengths can be weakly coupled, whereas long wavelengths are always strongly coupled. It is also worth recalling here that non perturbative features may arise in a system from the cooperation of many degrees of freedom, or strong classical fields, making the system strongly interacting while the elementary coupling strength remains small. An illustration is provided next.

6 High density partonic systems

The wave function of a relativistic system describes a collection of partons, mostly gluons, whose number grows with the energy of the system: this is because each gluon acts as a color source that can radiate other gluons when the system is boosted to higher energy (then x, the typical momentum fraction, decreases). This phenomenon has been well established at HERA [20]. One expects, however, that the growth of the gluon density eventually "saturates" when non linear QCD effects start to play a role. The existence of such a saturation regime has been predicted long ago, but it is only during the last decade that equations providing a dynamical description of this regime have been obtained (for recent reviews, see [21, 22, 23]).

The onset of saturation is characterized by a particular momentum scale, called the saturation momentum Q_s, given by $Q_s^2 \approx \alpha_s(Q_s^2) xG(x, Q_s^2)/\pi R^2$, where R is the transverse size of the system. Partons in the wave function have different transverse momenta k_T. Those with $k_T > Q_s$ are in a dilute regime; those with $k_T < Q_s$ are in the saturated regime. Note that at saturation, naive perturbation theory breaks down, even though $\alpha_s(Q_s)$ may be small if Q_s is large: the saturation regime is a regime of weak coupling, but large density. In fact, at saturation, the number of partons occupying a small disk of radius $1/Q_s$ in the transverse plane is proportional to $1/\alpha_s$, a large number if α_s is small. In such conditions classical field approximations become relevant to describe the nuclear wave-functions. This observation is at the basis of the McLerran-Venugopalan model [24]. The color glass formalism provides a more complete physical picture, allowing in particular a complete description of the evolution of the wave function as a function of energy [21, 22, 23].

The saturation momentum increases as the gluon density increases. This increase of the gluon density may come from the decrease of x with increasing energy ($Q_s^2 \sim x^{-0.3}$), or from the additive contributions of several nucleons in a nucleus, $xG_A(x, Q_s^2) \propto A$, and hence $Q_s^2 \propto \alpha_s A^{1/3}$, where A is the number of nucleons in the nucleus. Thus, the saturation regime sets in earlier (i.e., at lower energy) in collisions involving large nuclei than in those involving protons. In fact, the parton densities in the central rapidity region of a Au-Au collision at RHIC are not too different from those measured in deep inelastic scattering at HERA. In a nucleus-nucleus collision, most partons that play a direct role in particle production have momenta of the order of Q_s. A very successful phenomenology based on the saturation picture has been developped at RHIC (see e.g. [23, 25, 26] for recent reviews). However, understanding how the quark-gluon plasma is produced, i.e., understanding the detailed mechanisms by which partonic degrees of freedom get freed and subsequently interact to lead to a thermalized system, remains a challenging problem.

By selecting particular kinematics, one may reach lower values of x. Thus, for instance, the study of dA collisions at RHIC, in the fragmentation region of the deuteron, gives access to a regime of small x values in the nucleus, where quantum evolution could be significant. Indeed, very exciting results have been obtained in this regime [27], which have been interpreted as evidence of saturation (see e.g. [28, 23]). In particular, the disappearance of di-hadron correlations at forward rapidity, which has been observed recently [29], has a natural interpretation in terms of saturation. This result is potentially very important as it may represent the first direct evidence of large parton density effects [30].

7 Conclusion

The field of ultra-relativistic heavy ion collisions has undergone spectacular progress in the last decade, both theoretically and experimentally. Progress in understanding the behavior of QCD in the regime of large parton densities has contributed to bring together the field of small x physics, and that of heavy ions, and has led to very exciting developments. Other, somewhat unexpected, developments took place, such as the intrusion of string theoretical techniques and the use of the AdS/CFT duality in order to study strongly coupled plasmas. But, to a large extent, experiments continue to drive the field. As I have indicated, RHIC has produced a vast amount of high quality data which have forced us to revise our concepts, and left us with a number of puzzles. We can be confident that many of these puzzles will be clarified by the forthcoming experiments at the Large Hadon Collider.

References

[1] RHIC collaborations "white papers", Nucl. Phys. **A757** (2005).

[2] R. Bellwied, these proceedings.

[3] P. Braun-Munzinger and J. Wambach, arXiv:0801.4256 [hep-ph].

[4] K. Fukushima and T. Hatsuda, arXiv:1005.4814 [hep-ph].

[5] L. McLerran and R. D. Pisarski, Nucl. Phys. A **796** (2007) 83 [arXiv:0706.2191 [hep-ph]].

[6] J. P. Blaizot, E. Iancu and A. Rebhan, Phys. Rev. D **63** (2001) 065003 [arXiv:hep-ph/0005003]; Nucl. Phys. A698 (2002) 404.

[7] G. Endrodi, Z. Fodor, S. D. Katz and K. K. Szabo, PoS **LAT2007** (2007) 228 [arXiv:0710.4197 [hep-lat]].

[8] Y. Aoki, G. Endrodi, Z. Fodor, S. D. Katz and K. K. Szabo, Nature **443** (2006) 675 [arXiv:hep-lat/0611014].

[9] Z. Fodor, PoS **LAT2007** (2007) 011 [arXiv:0711.0336 [hep-lat]].

[10] A. Bazavov *et al.*, Phys. Rev. D **80** (2009) 014504 [arXiv:0903.4379 [hep-lat]].

[11] S. Borsanyi, Z. Fodor, C. Hoelbling, S. D. Katz, S. Krieg, C. Ratti and K. K. Szabo [Wuppertal-Budapest Collaboration], arXiv:1005.3508 [hep-lat].

[12] J. Adams *et al.* [STAR Collaboration], Phys. Rev. Lett. **91** (2003) 072304 [arXiv:nucl-ex/0306024].

[13] Y. Akiba [PHENIX Collaboration], Nucl. Phys. A **774** (2006) 403 [arXiv:nucl-ex/0510008].

[14] A. Majumder, J. Phys. G **34** (2007) S377 [arXiv:nucl-th/0702066].

[15] J. Y. Ollitrault, Phys. Rev. D **46**, 229 (1992).

[16] M. Luzum and P. Romatschke, Phys. Rev. C **78**, 034915 (2008) [Erratum-ibid. C **79**, 039903 (2009)] [arXiv:0804.4015 [nucl-th]].

[17] G. Policastro, D. T. Son and A. O. Starinets, Phys. Rev. Lett. **87** (2001) 081601 [arXiv:hep-th/0104066].

[18] P. Kovtun, D. T. Son and A. O. Starinets, Phys. Rev. Lett. **94** (2005) 111601 [arXiv:hep-th/0405231].

[19] S. S. Gubser, arXiv:0907.4808 [hep-th].

[20] S. Chekanov *et al.* [ZEUS Collaboration], Phys. Rev. D **67**, 012007 (2003) [arXiv:hep-ex/0208023].

[21] E. Iancu and R. Venugopalan, arXiv:hep-ph/0303204.

[22] H. Weigert, Prog. Part. Nucl. Phys. **55**, 461 (2005) [arXiv:hep-ph/0501087].

[23] J. Jalilian-Marian and Y. V. Kovchegov, Prog. Part. Nucl. Phys. **56** (2006) 104 [arXiv:hep-ph/0505052].

[24] L. D. McLerran and R. Venugopalan, Phys. Rev. D **49** (1994) 2233 [arXiv:hep-ph/9309289].

[25] F. Gelis, E. Iancu, J. Jalilian-Marian and R. Venugopalan, arXiv:1002.0333 [hep-ph].

[26] T. Lappi, arXiv:1003.1852 [hep-ph].

[27] I. Arsene *et al.* [BRAHMS Collaboration], Phys. Rev. Lett. **93** (2004) 242303 [arXiv:nucl-ex/0403005].

[28] D. Kharzeev, Y. V. Kovchegov, and K. Tuchin, *Phys. Lett.* B599:23–31, 2004.

[29] E. Braidot [STAR Collaboration], arXiv:1005.2378 [hep-ph].

[30] J. L. Albacete and C. Marquet, arXiv:1005.4065 [hep-ph].

Heavy ion physics with the ATLAS detector

Helena Santos for the ATLAS Collaboration

LIP, Av. Elias Garcia 14-1, 1000-149 Lisboa, Portugal

DOI: http://dx.doi.org/10.3204/DESY-PROC-2010-01/233

The ATLAS experiment will participate in the heavy ion program of the Large Hadron Collider (LHC), for which the main goal is to create strong interacting matter under extreme energy density and temperature conditions. Evidence from SPS and RHIC data suggests that in such extreme conditions matter undergoes a phase transition from ordinary hadronic matter to a plasma of quarks and gluons, the QGP. The large acceptance, high granularity calorimeters, silicon tracking detectors, and muon spectrometers assure that ATLAS can handle such a challenging program.

1 Introduction

Pb+Pb collisions at the LHC are expected to produce a QGP with energy densities 2–3 times (or even more) larger than at RHIC, with larger initial temperatures (by a factor of 2) and longer lifetimes (the order of 1.5). To carry on this program, the ATLAS [1] experiment has a large detector acceptance, as shown in Figure 1, with full azimuthal coverage and 10 units of pseudo-rapidity, not taking into account the very forward detectors which will play a major role in the heavy ion program. In Pb+Pb collisions, the detector is especially suited to study jets and photons. Concerning jets, the large acceptance and fine segmentation allows full reconstruction and a detailed study of their properties. For photons, the fine segmentation of the first layer of the electromagnetic calorimeter allows for separation of direct photons from those originating from π^0 and η decays. This is a unique strength of the ATLAS detector at the LHC.

2 Global observables

The day-one physics will be devoted to establish the global features of the heavy ion program. The collisions centrality is characterized event-by-event by the impact parameter, b, which is intrinsically related to the geometry of the collision and so to the number of collisions and the number of excited participating nucleons. A strong correlation between these variables and the energy deposited in the ATLAS calorimeters is expected. Figure 2 (left plot) demonstrates how well ATLAS reconstructs the transverse energy over the whole pseudorapidity range in central collisions, b=2 fm, taking into account correction factors for acceptance cracks and energy depositions by particles which originate from re-interactions in the detector material. Measurements of the inclusive charged particle density will be essential and few days of data taking will help establish which physics scenarios can be ruled out using the measured multiplicities [2]. The middle plot of Figure 2 shows the capabilities of ATLAS to reconstruct $dN_{ch}/d\eta$ in central collisions. The estimated errors are 10-15%.

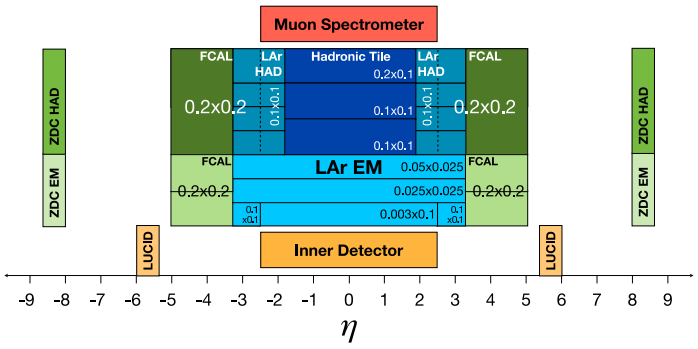

Figure 1: The pseudo-rapidity coverage of the various components of the ATLAS detector.

One observable that gives insight into the very earliest phase of the collisions is the elliptic flow, which arises when two colliding nuclei do not overlap totally. In such a case, the initial spatial anisotropy leads to a final state elliptical asymmetry in momentum space with respect to the reaction plane. The variable v_2 is the second Fourier coefficient of the particle azimuthal distribution with respect to the reaction plane and measures the elliptical shape of the particle's momentum distribution in the transverse plane. Figure 2 (right plot) shows v_2 as a function of the transverse momentum for mid-central events. Three methods to measure elliptic flow are applied to the simulated data – event plane, two-particle correlations and Lee-Yang Zeros [3, 4]. All three fail at the very low p_T due the presence of fake tracks in this momentum range. The Lee-Yang Zeros method, however, shows the best performance and is less sensitive to non-flow effects.

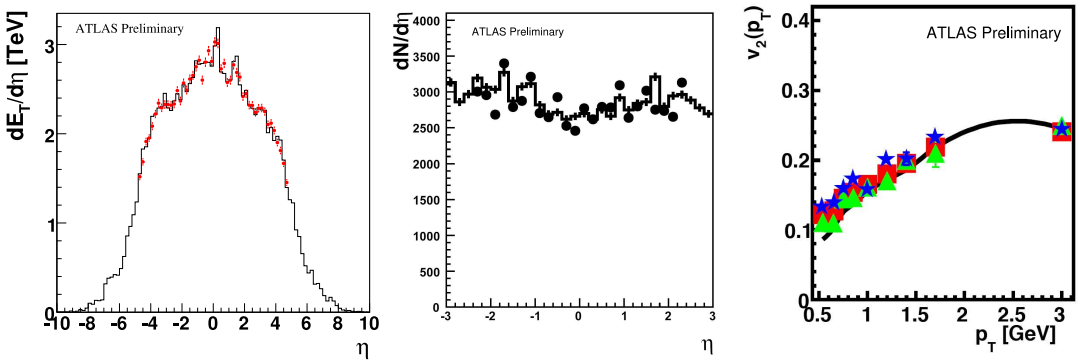

Figure 2: Left and middle: comparison of the reconstructed $dE_T/d\eta$ and $dN_{ch}/d\eta$ distributions (points) with the true distributions (histograms) for central events with b = 2.3 fm. Right: p_T dependence of the reconstructed v_2 from the event plane method (squares), two-particle correlations (stars) and the Lee-Yang Zeros method (triangles) for mid-central events, b=7 fm.

3 Jets

One of the most important topics of the LHC heavy ion program will be the jet suppression measurements [5, 6]. Jets reconstruction in Pb+Pb collisions is challenging due to the large underlying event. Thus, methods have been developed to subtract it by removing the averaged transverse energy, estimated far enough from the seeded jet signal, as well as to identify and reject fake jets [7, 8]. Figure 3 compares the reconstructed jet spectrum with the input one, and the fake jet spectrum as a function of the transverse energy. Even without correcting for efficiency and energy resolution, the reconstructed spectrum matches the input one above 80 GeV quite well. The background at low E_T is suppressed by two orders of magnitude. At 70 GeV the reconstruction efficiency is about 70%, the resolution is approximately 25% and the background is negligible.

4 Direct photons

The design of the ATLAS electromagnetic calorimeter is optimal for direct photon identification [1]. As seen in Figure 4, the first layer has a very fine longitudinal segmentation along the η direction, allowing to disentangle direct photons from π^0 and η photon decays. This is a unique feature of ATLAS and rather important because direct photons are not affected by the strong interacting medium and so they can be used as a reference for jet suppression measurements [5]. Also the energy scale determination will benefit because the p_T-balance of di-jet correlations is of limited use due to the expected energy loss in the QGP and the fluctuations of the large underlying event. The left plots of Figure 4 show the reconstructed energy deposition in the strip layers as a function of the strip cluster size, $\Delta\eta$, for direct photons and for π^0s embedded in HIJING central events. The energy of a single photon is concentrated across a few strips with a single maximum at the middle, whereas a cluster from a π^0 decay is distributed across more strips.

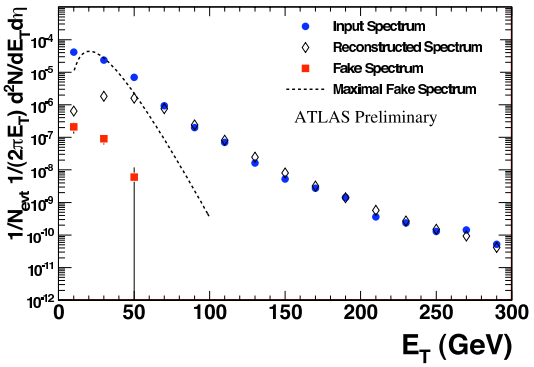

Figure 3: Input, raw reconstructed and fake spectra for cone jets in central ($dN_{ch}/d\eta$=2650) Pb+Pb collisions. The reconstructed spectrum is not corrected for efficiency and energy resolution. Dashed line represents the absolute fake jet rate from HIJING events prior to background jet rejection.

5 Heavy ions run in 2010

The first heavy ion run at the LHC is scheduled for November and December of 2010. The CM energy will be 2.76 TeV/nucleon pair, a factor 2 smaller than the nominal one. The peak luminosity will be 2 orders of magnitude smaller, 1–2x10^{25}. Taking into account the total inelastic Pb+Pb cross section, 7.7 barns, an interaction rate of 80-160 Hz is expected. Some

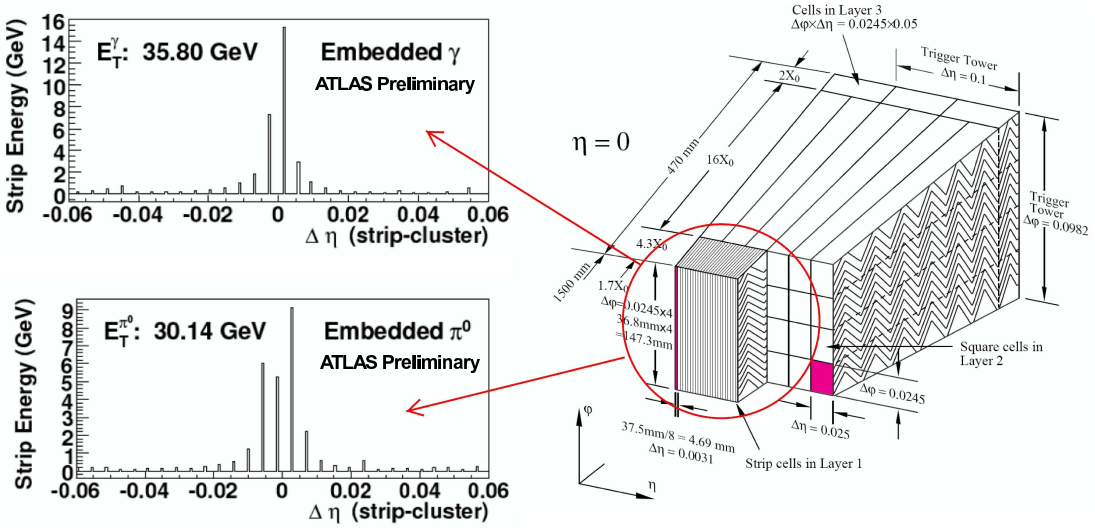

Figure 4: The reconstructed energy deposition in the strip layers around the direction of (top left) a single photon and a single π^0 (bottom left), both embedded in a central Pb+Pb event. On the right the sketch of a barrel module with the different layers is shown, with the fine granularity in η of the first layer being enhanced.

advantages of these low rates can be exploited, namely in triggering. In principle, depending on how large events will be, no Level-1 rejection is needed and the High Level Trigger will work in transparent mode. Beyond minimum bias, the Level-1 trigger will be used to find regions of interest concerning rare signals, namely jets, muons, and ultra-peripheral collisions. Even with low to moderate luminosity, 50 Hz written to tape will amount to two million Pb+Pb events per day.

In conclusion, ATLAS is fully prepared to collect and analyze the first heavy ion data.

6 Acknowledgments

This work was supported in part by FCT, UE, COMPETE, and QREN under the contract Project CERN/FP/109323/2009.

References

[1] The ATLAS Collaboration, G. Add et al., JINST 3, S08003 (2008).
[2] B. B. Back et al. PHOBOS Collaboration, Phys. Rev. C74, 021902 (2006a).
[3] S. Wang et al., Phys. Rev. C44, 1091 (1991) and references therein.
[4] R. S. Bhalerao, N. Borghini, and J. Y. Ollitrault, 4 Phys. Lett. B580, 157 (2004).
[5] S.S. Adler et al. PHENIX Collaboration, Phys. Rev. C75, 024909 (2007a).
[6] J. Adams et al. STAR Collaboration, Phys. Rev. Lett. 91, 072304 (2003).
[7] N. Grau for the ATLAS Collaboration, J. Phys. G: Nucl. Part. Phys. 35, 104040 (2008).
[8] N. Grau, B.A. Cole, W.G. Holzmann, M. Spousta and P. Steinberg for the ATLAS Collaboration, arXiv:0810.1219.

Posters

Unnatural Origin of Fermion Masses for Technicolor

Matti Antola[1], *Matti Heikinheimo*[2]*, *Francesco Sannino*[3], *Kimmo Tuominen*[4]

[1]Department of Physics and Helsinki Institute of Physics, P.O.Box 64, FI-000140, University of Helsinki, Finland
[2]Department of Physics, P.O.Box 35, FI-000140, University of Jyväskylä and Helsinki Institute of Physics, P.O.Box 64, FI-000140, University of Helsinki, Finland
[3]CP[3]-Origins, Campusvej 55, DK-5230 Odense M, Denmark
[4]CP[3]-Origins, Campusvej 55, DK-5230 Odense M, Denmark and Helsinki Institute of Physics, P.O.Box 64, FI-000140, University of Helsinki, Finland

DOI: http://dx.doi.org/10.3204/DESY-PROC-2010-01/heikinheimo

We explore the scenario in which the breaking of the electroweak symmetry is due to the simultaneous presence and interplay of a dynamical sector and an unnatural elementary Higgs. Here the elementary Higgs represents the sector responsible for fermion masses. Our goal is to investigate the interplay between the technicolor sector and the sector giving masses to the SM fermions, and this simple model works as a well defined framework that permits perturbative calculations.

The idea of bosonic technicolor was originally pioneered in a series of papers by Simmons [1], Kagan and Samuel [2] and Carone and Georgi [3, 4]. More recently this type of model has been investigated also in [5]. It was noted that these models permit to write renormalizable Yukawa interactions with ordinary fermions replacing the extended technicolor dynamics. In comparison to the earlier works we have:

- Included all dimension four operators with at most one mixing between the two scalar sectors.
- Provided an extensive scan of the parameters of the model.
- Updated the comparison with measurements.
- We linked the dynamical sector with models of (Ultra) Minimal Walking technicolor [6, 7, 8, 9].

We start with the following Lagrangian:

$$\mathcal{L}_{UTC} = \mathcal{L}_{SM}\Big|_{\text{Higgs}=0} + \mathcal{L}_{TC} + \mathcal{L}_{\text{Higgs}} + \mathcal{L}_{\text{Yukawa}} \,. \tag{1}$$

The TC-sector has no direct couplings with the SM fermions, but the elementary Higgs has Yukawa couplings with both the SM- and technifermions, encoded in $\mathcal{L}_{\text{Yukawa}}$. We construct

*Speaker

a low energy effective theory, where both the composite and the elementary scalar sector are described by a linear Lagrangian. The composite field is written as

$$M = \frac{1}{\sqrt{2}}\left(sI_{2\times 2} + 2i\pi_M\right) \propto Q_L \bar{Q}_R, \quad \langle s\rangle \equiv f, \tag{2}$$

where f is the technipion decay constant, and the elementary Higgs field as

$$H = \frac{1}{\sqrt{2}}\left(hI_{2x2} + 2i\pi_H\right), \quad \langle h\rangle \equiv v\ . \tag{3}$$

The Higgs Lagrangian is then given by

$$\mathcal{L}_{\rm Higgs} = \frac{1}{2}Tr\left[DH^\dagger DH\right] - V_H,\ V_H = \frac{1}{2}m_H^2 Tr\left[H^\dagger H\right] + \frac{\lambda_H}{4!}Tr^2\left[H^\dagger H\right]. \tag{4}$$

The technicolor sector is taken to be the Next to Minimal Walking Technicolor (NMWT) model [7], consisting of two techniflavors in the two-index symmetric representation of $\mathrm{SU}(3)_{\rm TC}$.

The techniquark Yukawa term

$$-\bar{Q}_L H Y_Q Q_R, \tag{5}$$

breaks the $(\mathrm{SU}(2)_{\rm L}\times\mathrm{SU}(2)_{\rm R})^2$ global symmetry of the model down to $\mathrm{SU}(2)_{\rm R}\times\mathrm{U}(1)_{\rm R}$. As the techniquarks form the chiral condensate, this term yields a linear term in the elementary scalar Lagrangian that will generate a vacuum expectation value for the Higgs, regardless of the sign of the original mass term m_H^2. When constructing the effective Lagrangian that mixes the technicolor sector with the elementary scalar, we include all dimension four operators with at most one mixing between the two scalar sectors. Applying Georgi's generalized naive dimensional analysis [10] we arrive at the following Lagrangian for the TC-sector and its coupling with the elemantary Higgs:

$$\begin{aligned}
\mathcal{L}_{TC} - \bar{Q}_L H Y_Q Q_R \quad &\rightarrow \quad \frac{1}{2}\mathrm{Tr}\left[DM^\dagger DM\right] + \frac{1}{2}(c_3/\alpha)\mathrm{Tr}\left[DM^\dagger DHY_Q\right] - V_M \\
V_M \quad &= \quad \frac{1}{2}m_M^2\mathrm{Tr}\left[M^\dagger M\right] + \frac{\lambda_M}{4!}\mathrm{Tr}^2\left[M^\dagger M\right] \\
&\quad -\frac{1}{2}(\alpha c_1)f^2\mathrm{Tr}\left[M^\dagger HY_Q\right] - \frac{1}{24}(\alpha c_2)\mathrm{Tr}\left[M^\dagger M\right]\mathrm{Tr}\left[M^\dagger HY_Q\right] \\
&\quad -\frac{1}{24}(c_4/\alpha)\mathrm{Tr}\left[H^\dagger H\right]\mathrm{Tr}\left[M^\dagger HY_Q\right] + \text{h.c.}
\end{aligned} \tag{6}$$

Here $c_1 \ldots c_4$ are order one dimensionless real coefficients and $\alpha = \Lambda/f$, where Λ is the mass of the lowest lying vector resonance of the theory, is taken to be greater than one.

The above Lagrangian is diagonalized, and the physical propagating fields are given by a non unitary transformation from the original fields, due to the kinetic mixing term. In unitary gauge, the particle spectrum consists of two SM Higgs -like scalars and three massive pions, while three massless pions have been eaten to become the longitudinal degrees of freedom of the weak gauge bosons.

We perform an extensive scan of the parameters of the model, not restricting to any special case for the mass parameter of the fundamental scalar, as opposed to earlier work on models of this type. We constrain the parameters via direct search limits and electroweak and flavor precision tests. The mass patterns for the two scalars, passing all the electroweak and flavor

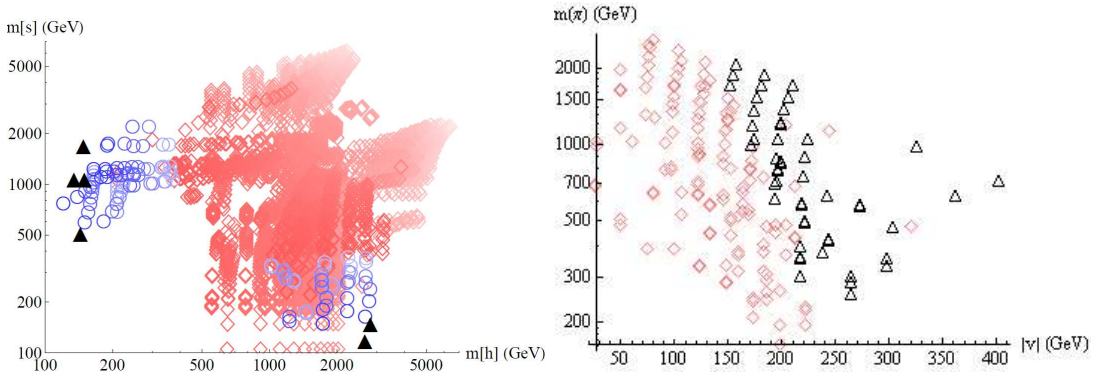

Figure 1: Left: The masses of the scalar particles. The black triangles are allowed by all data, blue circles are less favored by the electroweak precision data and red diamonds are ruled out. Right: The mass of the technipions, as a function of the vacuum expectation value of the elementary scalar. The black triangles are allowed and the read diamonds are ruled out.

tests as well as direct search limits, are shown as black triangles in the left panel of figure 1. Blue circles are less favored by the electroweak precision data and the red diamonds are ruled out. Our model thus predicts the existence of one light and one heavy Higgs-like scalar. The right panel of the figure shows as black triangles the allowed mass of the technipions, as a function of the vacuum expectation value of the elementary scalar. We see that the technipion mass is not very well constrained by the electroweak precision data, ranging from a few hundred GeV to a few TeV.

We find that the model is viable in the light of all existing experimental data and can be seen as a stepping stone towards a well defined extension of the SM featuring a complete solution to both the origin of spontaneous breaking of the electroweak symmetry and the mass of any SM fermion.

References

[1] E. H. Simmons, Nucl. Phys. B **312**, 253 (1989).

[2] A. Kagan and S. Samuel, Phys. Lett. B **270**, 37 (1991).

[3] C. D. Carone and E. H. Simmons, Nucl. Phys. B **397**, 591 (1993) [arXiv:hep-ph/9207273]; C. D. Carone and H. Georgi, Phys. Rev. D **49**, 1427 (1994) [arXiv:hep-ph/9308205].

[4] C. D. Carone, E. H. Simmons and Y. Su, Phys. Lett. B **344**, 287 (1995) [arXiv:hep-ph/9410242].

[5] A. R. Zerwekh, arXiv:0907.4690 [hep-ph].

[6] F. Sannino and K. Tuominen, Phys. Rev. D **71**, 051901 (2005) [arXiv:hep-ph/0405209].

[7] D. D. Dietrich, F. Sannino and K. Tuominen, Phys. Rev. D **72**, 055001 (2005) [arXiv:hep-ph/0505059]; D. D. Dietrich, F. Sannino and K. Tuominen, Phys. Rev. D **73**, 037701 (2006) [arXiv:hep-ph/0510217].

[8] D. D. Dietrich and F. Sannino, Phys. Rev. D **75**, 085018 (2007) [arXiv:hep-ph/0611341]. T. A. Ryttov and F. Sannino, Phys. Rev. D **76**, 105004 (2007) [arXiv:0707.3166 [hep-th]].

[9] T. A. Ryttov and F. Sannino, Phys. Rev. D **78**, 115010 (2008) [arXiv:0809.0713 [hep-ph]].

[10] H. Georgi, Phys. Lett. B **298** (1993) 187 [arXiv:hep-ph/9207278].

Collider signatures related to quark flavour violation in the MSSM

Björn Herrmann

DESY, Notketraße 85, 22607 Hamburg, Germany

in collaboration with A. Bartl, M. Bruhnke, H. Eberl, K. Hidaka, W. Majerotto and W. Porod

DOI: http://dx.doi.org/10.3204/DESY-PROC-2010-01/herrmann

In the Standard Model (SM), the only source of flavour violation are the Yukawa interactions and the resulting rotation from the gauge to the mass eigenstates of the fermions. In consequence, all quark-flavour violating (QFV) interactions can be parametrized in terms of the CKM-matrix. Among the numerous extensions of the SM, Supersymmetry (SUSY) and in particular the Minimal Supersymmetric Standard Model (MSSM) is among the most popular and best-studied ones. Postulating a superpartner with opposite statistics for each of the SM particles, it cures the hierarchy problem by stabilizing the Higgs mass, leads to gauge coupling unification, and includes interesting candidates for the cold dark matter observed in our Universe. Although it is clear that SUSY must be broken at the electroweak scale, there is no theoretical consensus about the exact breaking mechanism. One therefore introduces so-called soft-breaking terms in the SUSY Lagrangian.

One of the open questions related to the breaking mechanism concerns the flavour structure of the theory. The hypothesis of minimal flavour violation (MFV) assumes that flavour violation is the same as in the SM. Then, all QFV interactions (e.g. the squark-quark-chargino vertex) are again parameterized through the CKM-matrix. However, new sources of flavour violation can appear in SUSY models, especially if they are embedded in larger frameworks such as grand unified theories. This non-minimal flavour violation (NMFV) allows then for non-diagonal – i.e. flavour-violating – entries in the mass matrices of the sfermions that are not related to the CKM-matrix any more. These entries are conveniently considered as additional free parameters at the electroweak scale and can imply a different phenomenology as compared to the case of MFV. For a review on flavour violation in the MSSM see, e.g., Ref. [1]. Details on the parametrization of NMFV in the MSSM can also be found in Refs. [2, 3, 4, 5].

The studies discussed in the following focus on NMFV in the sector of squarks. Analogous arguments hold for sleptons, where the CKM-matrix is replaced by the PMNS-matrix. Moreover, the present analyses are based on flavour-mixing between the second and third generation and within the right-right sector of the squark mass matrices, which are least constrained by experimental measurements. The benchmark scenario SPS1a' [6], which serves as input for many experimental studies, is taken as reference point within the framework of minimal supergravity. The observed features are, however, present in wide ranges of the MSSM parameter space and also for variations of other QFV entries in the mass matrices.

Experimental limits from a large variety of rare decays, meson oscillations, or other precision measurements put strong constraints on the QFV elements of the squark mass matrices. Most

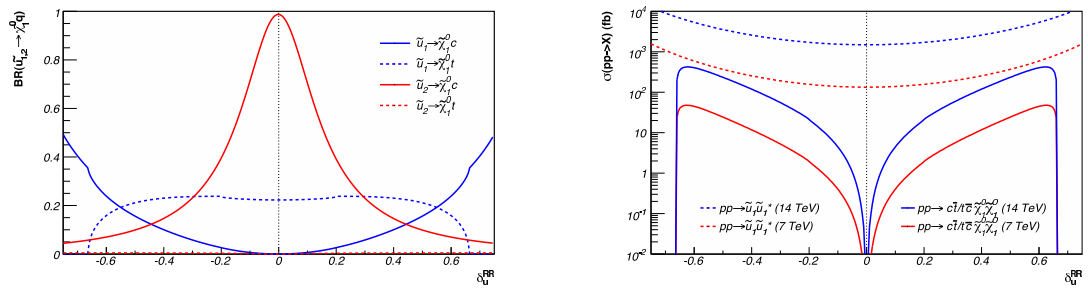

Figure 1: Branching ratios (left) of the two lightest up-type squarks and production cross-sections (right) of the discussed NMFV-signature for squark generation mixing between the second and third generations.

important in the context of QFV are the decays $b \to s\gamma$ and $b \to s\mu\mu$ as well as the observable ΔM_{B_s} related to B-meson oscillations. In the present study, all relevant constraints have explicitly been taken into account at the 95% confidence level and combined with the theoretical error estimate where available. Detailed discussions of the resulting allowed regions are given in Refs. [2, 3, 4, 5, 7, 8].

The physical mass spectrum of the squarks strongly depends on the introduced flavour-violating elements of the mass matrices [2, 4, 5, 7, 8]. In particular, the mass splitting between the involved mass eigenstates is increased with increasing flavour mixing. At the same time, the flavour content of the different squarks is modified. For example, the lightest up-type squark is a pure stop-mixture in the case of MFV, but receives sizeable charm-admixtures for larger values of the corresponding non-diagonal entries in the mass matrix. Vice versa, the charm content of the second-lightest squark is then exchanged for a stop-admixture.

The modified mass spectrum and flavour contents alter the decay modes of the squarks. In particular, new channels can be opened when introducing NMFV-elements in the mass matrices [4, 5]. The left panel of Fig. 1 shows the example of the fermionic decays of the two lightest up-type squarks into neutralinos. Here and in the following, the variables δ_u^{RR} and δ_d^{RR} parametrize the mixing (in the right-right sector) between the second and third generation up- and down-type squarks, respectively. The non-diagonal elements of the squark mass matrix are normalized to the diagonal ones according to Refs. [4, 5]. For a wide range of the NMFV-parameter, at least three of the branching ratios are simultaneously large, which may lead to important QFV effects in collider experiments [4].

In particular, they can give rise to sizeable event rates for the signal

$$pp \to \tilde{u}_{1,2}\tilde{u}^*_{1,2} \to c\bar{t}\ (t\bar{c})\ \tilde{\chi}^0_1\tilde{\chi}^0_1,$$

where the neutralinos give rise to missing transverse energy ($E_T^{\rm miss}$). While this process is practically not realized in the MSSM with MFV or in the Standard Model, allowing for NMFV can lead to rather sizeable cross-sections already for a moderate amount of additional flavour-mixing, as can be seen in the right panel of Fig. 1. The expected number of signal events at the LHC would be up to about 20.000 (10) for an integrated luminosity of 100 fb^{-1} (1 fb^{-1}) at $\sqrt{s} = 14$ TeV (7 TeV) [4].

Concerning the detectibility, top-quark identification is necessary to distinguish the proposed signal from top-antitop production including missing energy. The most crucial point for flavour-

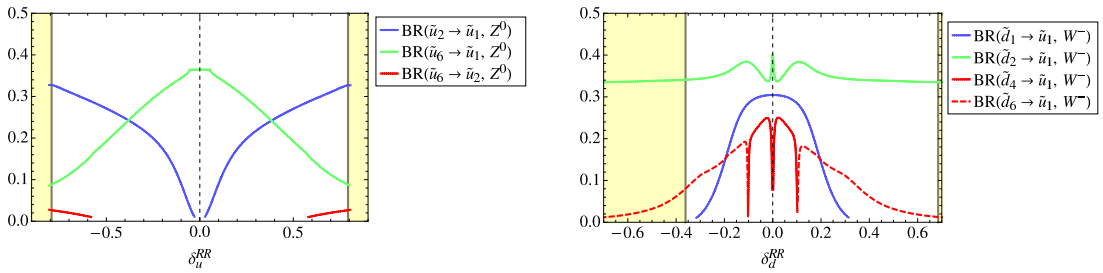

Figure 2: Typical NMFV-signatures related to squarks decaying into Z- or W-bosons for generation mixing between the second and third generations.

mixing between the second and third generation would be efficient charm-tagging. Otherwise, one should rather search for the signature $jet + (anti)top + E_T^{\rm miss}$ [4].

Another type of NMFV-signature at colliders is connected to the bosonic decay modes of the squarks [5]. As for the fermionic case discussed above, new channels can be opened when allowing for new flavour-mixing entries in the mass matrices. Fig. 2 shows the example for decays of selected squarks into Z- or W-bosons and an up-type squark. Assuming MFV, only one squark can decay into the final state $\tilde{u}_1 Z^0$ in the given example. For increasing non-minimal flavour-mixing, as discussed above, a second mass eigenstate obtains a sizeable stop-content. At the same time, the mass of the lightest squark $\tilde{u}_1$ is decreasing so that the new decay channel $\tilde{u}_6 \to \tilde{u}_1 Z^0$ is opened [5].

Similar arguments hold for the decay of squarks into W-bosons. Here, two modes are present for MFV, while additional channels become possible already for moderate flavour-violating entries. If it will be possible to observe squarks at the LHC and to reconstruct their decays modes, the observation of such a signature would exclude the hypothesis of MFV [5].

In summary, despite the strong constraints from experimental data, NMFV can lead to new signatures in collider experiments that can challenge the hypothesis of MFV. Here, this has been shown for the benchmark scenario SPS1a'. The given conclusions hold, however, for wide ranges of the MSSM parameter space [4, 5]. The presented results are a clear call for detailed Monte-Carlo studies including background reactions and detector simulation. Such studies will in particular be necessary to identify the regions of parameter space where the proposed signatures are observable.

References

[1] F. del Aguila *et al.*, Eur. Phys. J. C57: 183 (2008).

[2] T. Hurth and W. Porod, JHEP 0908: 067 (2009).

[3] A. Bartl, K. Hidaka, K. Hohenwarter-Sodek, T. Kernreiter, W. Majerotto and W. Porod, Phys. Lett. B679: 260 (2009).

[4] A. Bartl, H. Eberl, B. Herrmann, K. Hidaka, W. Majerotto, W. Porod, arXiv:1007.5483 [hep-ph].

[5] M. Bruhnke, B. Herrmann and W. Porod, accepted for publication in JHEP, arXiv:1007.2100 [hep-ph].

[6] J. A. Aguilar-Saavedra *et al.*, Eur. Phys. J. C46: 43 (2006).

[7] G. Bozzi, B. Fuks, B. Herrmann and M. Klasen, Nucl. Phys. B787: 1-52 (2007).

[8] B. Fuks, B. Herrmann and M. Klasen, Nucl. Phys. B810: 266-299 (2008).

ATLAS high-level calorimeter trigger algorithms performance with first LHC *pp* collisions

Pavel Jež for the ATLAS Collaboration

Niels Bohr Institute, Blegdamsvej 17, 2100 Copenhagen, Denmark

DOI: http://dx.doi.org/10.3204/DESY-PROC-2010-01/jez

After the commissioning phase with beams at SPS injection energy (450 GeV), the LHC [1] recently started the physics program with 7 TeV collisions. Consequently, the ATLAS detector [2] also entered its operation phase recording these collisions.

The task of the ATLAS trigger is to select 200 events out of 40 millions every second. It starts with the hardware-based trigger, the Level 1 (L1), which finds Regions of Interest (RoI's) using coarse information from the fast muon chamber or calorimeter. These RoI's are used as starting points for the two software based trigger levels: the Level 2 (L2), which operates only in the RoI's but uses full detector granularity, and the Event Filter (EF), which can explore the whole detector using full granularity information. The L2 and the EF are altogether referred to as the High Level Trigger (HLT) system. The L1 output rate is roughly 75 kHz with a latency of 2.5 μs. At L2, the output rate is decreased to 3 kHz with 40 ms latency and finally the EF output is 200 Hz and the time budget is roughly 4 s per event.

All trigger algorithms share a common data preparation step, optimized for fast processing. During the initial data taking period while the nominal luminosity is not attained, the trigger system accepts most of the incoming events and the bulk of the selection is performed only by the L1. The HLT is functional, but its decision is used for event rejection only when the maximum recording rate is reached. The trigger menus are composed of several signature subtriggers specialized in selecting different event types. Those using calorimeter data are presented in this paper.

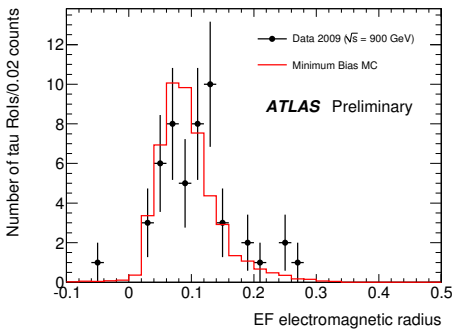

Figure 1: Candidate τ jet EM radius distribution at EF. Dots are 2009 collision data, solid line is MC expectation.

For example, the τ trigger is designed to select hadronic decays of the τ lepton, characterized by the presence of 1 or 3 $\pi^{\pm}$ accompanied by a ν and possibly π^0's. At L1, the τ trigger uses the electromagnetic (EM) and hadronic calorimeter to find transverse energy (E_T) deposits which pass the threshold (lowest is 5 GeV). At L2, selection criteria are applied using tracking and calorimeter based information. This takes advantage of calorimeter cluster confinement and low track multiplicity to discriminate τ's from the multi-jet background. Exploiting the same characteristics, the EF uses different selection criteria for single-prong (1 $\pi^{\pm}$) and multi-prong (3 $\pi^{\pm}$) decays in more refined algorithms which are almost identical to the offline reconstruction algorithms.

The distributions of the important observables obtained from data during 2009 have been compared with the non-diffractive minimum bias Monte Carlo and show reasonable agreement given the limited statistics. Fig. 1 presents a measure of the shower lateral size in the EM calorimeter (EM radius) calculated by the EF as the energy-weighted average cell distance from the cluster barycenter (obtained after weighting the position of each cell by its energy). It is an important discriminating variable because τ jets are more confined than QCD jets. Note that in all figures the MC has been normalized by the number of entries in data sample.

The ATLAS jet trigger is based on the selection of high hadronic E_T depositions. If a L1 jet candidate passes a given E_T threshold (lowest is 5 GeV), the L2 jet trigger continues by requesting calorimeter data around the L1 jet RoI position and runs an iterative cone algorithm with fixed radius. The EF jet algorithm is based on the offline reconstruction algorithm using calorimeter towers projecting towards the collision centre.

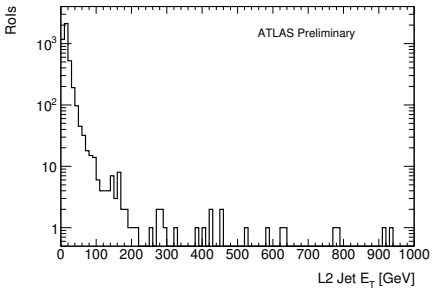

Figure 2: Transverse energy of jets measured at L2 in 900 GeV collisions.

The most important variable for the jet trigger is the transverse energy. The E_T measured in both the EM and the hadronic calorimeter is added up to obtain the jet trigger E_T. The distribution of the jet E_T obtained at L2 is presented in Fig. 2. Some clearly unphysical jets (with more than half the beam energy) are related to the detector noise. Jet clean-up procedures are being established by the collaboration to deal with such issues.

The aim of the e/γ trigger is to select events with electrons or photons in the final state. At L1, a threshold is set on minimal E_T deposit in the electromagnetic calorimeter (the lowest was 3 GeV in the commissioning period). At L2, fast algorithms for calorimeter reconstruction are run and fast tracking is used to reconstruct electron L2 objects. Already at this level it is possible to use the fine granularity of the first layer of the EM calorimeter to distinguish between primary and secondary γ's coming from π^0. At the EF, reconstruction algorithms very similar to those used offline are applied.

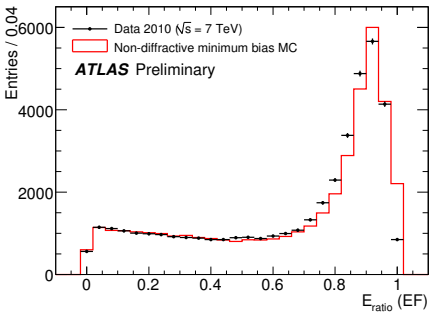

Figure 3: Distribution of photon E_{ratio} at EF. Dots are 7 TeV collision data, solid line is MC expectation.

Nice agreement with Monte Carlo expectation is observed with both 900 GeV and 7 TeV collisions. An important e/γ shower shape variable is called E_{ratio}, which is the fractional difference between the first and second highest energetic cell in the first calorimeter layer (Fig. 3 shows its distribution). For single γ's it peaks around 1, while for γ pairs from π^0 decays it is close to 0.

The ATLAS detector can be triggered also by events with considerable missing E_T or with a large amount of total E_T deposited in the calorimeters. That could play a crucial role in new physics discoveries such as dark matter candidates. The vector (missing E_T) and scalar (total E_T) sum of E_T are computed at L1 from all calorimeter elements. At L2, missing E_T is computed by adding the vector and scalar sums of all reconstructed muon momenta to the calorimetric measurement done at L1. Note that L2 is presently not configured to access L2

energy measurements due to strong network restrictions to read-out the whole detector at the full L2 input rate. At the EF, the total E_T and missing E_T are again recalculated with more precise input from the whole detector. Like for the other calorimeter triggers, no significant deviation from the MC expectation was observed in collision data. Figure 4 presents the comparison of minimum bias Monte Carlo and missing E_T measured at the EF from 7 TeV collisions. More details about the missing E_T trigger performance can be found in [3].

In order to guarantee the quality of the information provided at the trigger level, automatic monitoring is performed with respect to the information obtained offline. One of the most important tests is the comparison of energy of the clusters produced by the EF to the clusters produced by the offline code. Those checks verify that the cell and cluster calculations are compatible at both levels despite the different choice of algorithms or parameters.

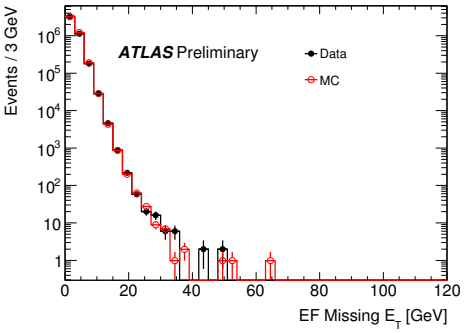

Figure 4: Distribution of missing E_T at EF. Dots are 7 TeV collision data, solid line is MC expectation.

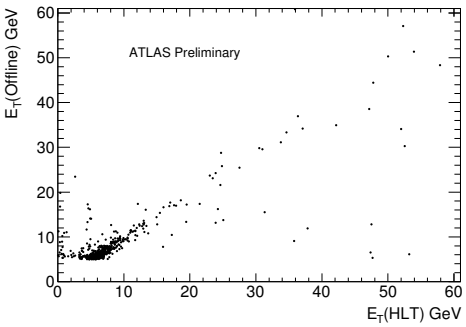

Figure 5: Correlation of the EF and offline E_T obtained from 900 GeV data.

The correlation of the E_T of e/γ clusters calculated at the EF and during offline reconstruction is presented on Fig. 5. Note that several off-diagonal candidates with low offline E_T and high EF E_T would not pass offline quality cuts which are used to declare the EM cluster to be an electron or photon candidate. More analyses are ongoing to produce even more HLT/offline compatible results.

The studies presented in this paper demonstrated that calorimeter HLT algorithms are under control. Key observables behave comparable to MC studies and ongoing comparison with offline performance shows no important bias caused by those algorithms. Furthermore, time requirements were evaluated to be within the required operational constraints and all algorithms proved their robustness during the many hours long LHC runs. A comprehensive summary of the calorimeter HLT performance as well as further references can be found in [4].

Recently, many of the algorithms (especially from e/γ and τ triggers) were switched to perform active selection of events during runs with higher luminosity.

References

[1] L. Evans and P. Bryant, JINST **3** (2008) S08001.
[2] G. Aad *et al.* [ATLAS Collaboration], JINST **3** (2008) S08003.
[3] G. Aad *et al.* [ATLAS Collaboration], ATLAS-CONF-2010-026.
[4] G. Aad *et al.* [ATLAS Collaboration], ATLAS-CONF-2010-030.

Three-loop predictions for the light Higgs mass in the MSSM

Philipp Kant

Humboldt-Universität zu Berlin, Newtonstr. 15, 12489 Berlin

DOI: http://dx.doi.org/10.3204/DESY-PROC-2010-01/kant

The Minimal Supersymmetric Extension of the Standard Model (MSSM) features a light Higgs boson, the mass M_h of which is predicted by the theory. Given that the LHC will be able to measure the mass of a light Higgs with great accuracy, a precise theoretical calculation of M_h yields an important test of the MSSM. In order to deliver this precision, we present three-loop radiative corrections of $\mathcal{O}\left(\alpha_t\alpha_s^2\right)$ and provide a computer code that combines our results with corrections to M_h at lower loop orders that are available in the literature.

1 Introduction

The Higgs sector of the Minimal Supersymmetric Extension of the Standard Model (MSSM) consists of a two-Higgs doublet model, which is tightly constrained by supersymmetry. In particular, the quartic terms of the Higgs potential are completely fixed by the gauge couplings. Thus, it is possible to describe the MSSM Higgs sector through only two new (with respect to the Standard Model) parameters, which are usually taken to be the mass M_A of the pseudoscalar Higgs and the ratio $\tan\beta = \frac{v_2}{v_1}$ of the vacuum expectation values of the Higgs doublets. In particular, M_h, the mass of the light scalar Higgs boson, can be predicted, and at the tree-level only these two parameters enter the prediction, leading to an upper bound of $M_h \leq M_Z$. However, M_h is sensitive to virtual corrections to the Higgs propagator that shift this upper bound significantly. These virtual corrections depend on all the supersymmetry breaking parameters. This sensitivity to virtual corrections, combined with the great precision with which the Large Hadron Collider (LHC) will be able to measure the mass of a light Higgs, allows M_h to be used as a precision observable to test supersymmetric models – assuming that the theoretical uncertainties are suffiently small and under control.

Consequently, the one- and two-loop corrections to M_h have been studied extensively in the literature (see, for example [1, 2, 3, 4, 5, 6, 7, 8]). The remaining uncertainty has been estimated to be about $3 - 5\,\text{GeV}$ [10, 9]. Recently, also three-loop corrections have become available. The leading- and next-to-leading terms in $\ln(M_{SUSY}/M_t)$, where M_{SUSY} is the typical scale of SUSY particle masses, have been obtained in [11]. Motivated by the observation that the contributions from loops of top quarks and their superpartners, the stops, are dominant at the one- and two-loop level, we have calculated three-loop SUSY-QCD corrections to these diagrams. These corrections are of $\mathcal{O}\left(\alpha_t\alpha_s^2\right)$, where α_t is the coupling of the Higgs to the top quarks. A first result has been obtained in [12]. There, we assumed that all the superpartners had approximately the same mass. This restriction has been dropped recently in [13].

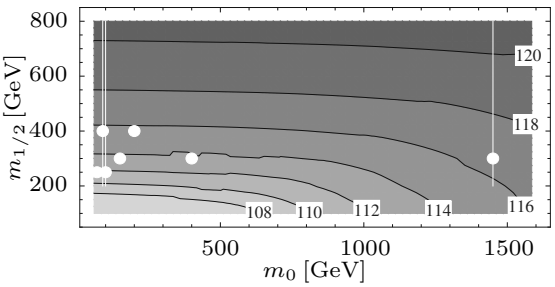

Figure 1: Prediction for the value of M_h (in GeV) for MSUGRA scenario with $\tan\beta = 10$, $A_0 = 0$, as evaluated by H3M. The white lines and points indicate the benchmark scenarios of [19].

2 Organisation of the calculation

A major difficulty in obtaining the results of [13] was the presence of many different mass scales – the masses m_t of the top quark, $m_{\tilde{g}}$ of the gluino, $m_{\tilde{t}_{1,2}}$ of the stops and $m_{\tilde{q}}$ of the partners of the light quarks – in the three-loop propagator diagrams. Assuming that there is a distinct hierarchy between these masses, they can be disentangled by the method of asymptotic expansions [14], yielding an expansion of the diagrams in small mass ratios and logarithms of mass ratios. Working in the effective potential approximation, we set the external momentum flowing through the Higgs propagator to zero and are left with tadpole integrals with a single mass scale, which are known and implemented in the FORM [15] program MATAD [16].

However, as the masses of the superpartners are not known, it is not clear which hierarchy one should assume. We solve this by computing the diagrams for many different hierarchies. Then, when given a point in the MSSM parameter space, we choose whichever hierarchy fits best and evaluate M_h using the calculation in the chosen hierarchy. To choose the best hierarchy and to estimate the error introduced by the asymptotic expansion, we compare, at the two-loop level, our expanded result with the result of [7], which contains the full mass dependence.

For convenience, we have written the MATHEMATICA package H3M [17], which automatically performs the choice of the best fitting hierarchy and provides a SUSY LES HOUCHES interface to our calculation. This allows to perform parameter scans as in Fig. 1. In order to get a state-of-the art prediction for M_h, we include all available contributions to M_h at the one- and two-loop level that are implemented in FEYNHIGGS [18]. For details on the usage and inner workings of the program, we refer to [13].

3 Estimating the theoretical uncertainty

We observe that the dependence of M_h on the renormalisation prescription, which is often used as a guesstimate for the uncertainty due to unknown higher order corrections, reduces drastically when one goes from two to three loops. But since we also find that the size of the three-loop corrections can be of the order of one to two GeV, which is rather large given that the two-loop corrections are only about a factor of two larger, we prefer to be conservative in our estimation of the theoretical uncertainty. Assuming a geometric progression of the perturbative series, we get for MSUGRA scenarios an uncertainty due to missing higher order corrections of 100 MeV to 1 GeV, depending on the value of $m_{1/2}$. The parametric uncertainty due to α_s, m_t

and $m_{\tilde{t}_{1,2}}$ is of the same order of magnitude. The uncertainty introduced by the expansion in mass ratios amounts to at most 100 MeV [13].

4 Conclusions

We present a calculation of the $\mathcal{O}\left(\alpha_t\alpha_s^2\right)$ corrections to M_h, shifting the value of M_h by about 1 GeV. We provide a computer code combining our results with corrections from lower loop orders, thus enabling a state-of-the-art prediction of M_h. Our calculation lowers the theoretical uncertainty due to missing higher orders to the same magnitude as the parametric uncertainty.

This work was supported by the DFG through SFB/TR 9 and by the Helmholtz Alliance "Physics at the Terascale".

References

[1] R. Hempfling and A. H. Hoang, Phys. Lett. B **331**, 99 (1994) [hep-ph/9401219]. H. E. Haber, R. Hempfling and A. H. Hoang, Z. Phys. C **75**, 539 (1997) [hep-ph/9609331].

[2] R.J. Zhang, Phys. Lett. B **447**, 89 (1999) [hep-ph/9808299]; J.R. Espinosa and R.J. Zhang, JHEP **0003**, 026 (2000) [hep-ph/9912236]; Nucl. Phys. B **586**, 3 (2000) [hep-ph/0003246].

[3] S. Heinemeyer, W. Hollik and G. Weiglein, Phys. Rev. D **58**, 091701 (1998) [hep-ph/9803277]. Phys. Lett. B **440**, 296 (1998) [hep-ph/9807423]. Eur. Phys. J. C **9**, 343 (1999) [hep-ph/9812472].

[4] A. Pilaftsis and C. E. Wagner, Nucl. Phys. B **553**, 3 (1999) [hep-ph/9902371]. M. Carena, J. R. Ellis, A. Pilaftsis and C. E. Wagner, Nucl. Phys. B **586**, 92 (2000) '[hep-ph/0003180], Nucl. Phys. B **625**, 345 (2002) [hep-ph/0111245].

[5] M. Carena et al, Nucl. Phys. B **580**, 29 (2000) [hep-ph/0001002].

[6] J. R. Espinosa and I. Navarro, Nucl. Phys. B **615**, 82 (2001) [hep-ph/0104047].

[7] G. Degrassi, P. Slavich and F. Zwirner, Nucl. Phys. B **611**, 403 (2001) [hep-ph/0105096], A. Brignole, G. Degrassi, P. Slavich and F. Zwirner, Nucl. Phys. B **631**, 195 (2002) [hep-ph/0112177], Nucl. Phys. B **643**, 79 (2002) [hep-ph/0206101].

[8] S. P. Martin, Phys. Rev. D **67** (2003) 095012 [arXiv:hep-ph/0211366].

[9] B. C. Allanach, A. Djouadi, J. L. Kneur, W. Porod and P. Slavich, JHEP **0409** (2004) 044 [arXiv:hep-ph/0406166].

[10] G. Degrassi, S. Heinemeyer, W. Hollik, P. Slavich and G. Weiglein, Eur. Phys. J. C **28**, 133 (2003) [arXiv:hep-ph/0212020].

[11] S. P. Martin, Phys. Rev. D **75** (2007) 055005 [arXiv:hep-ph/0701051].

[12] R. V. Harlander, P. Kant, L. Mihaila and M. Steinhauser, Phys. Rev. Lett. **100** (2008) 191602 [Phys. Rev. Lett. **101** (2008) 039901] [arXiv:0803.0672 [hep-ph]].

[13] P. Kant, R. V. Harlander, L. Mihaila and M. Steinhauser, arXiv:1005.5709 [hep-ph].

[14] V. A. Smirnov, Springer Tracts Mod. Phys. **177** (2002) 1.

[15] J. A. M. Vermaseren, arXiv:math-ph/0010025.

[16] M. Steinhauser, Comput. Phys. Commun. **134** (2001) 335 [arXiv:hep-ph/0009029].

[17] `http://www-ttp.particle.uni-karlsruhe.de/Progdata/ttp10/ttp10-23`

[18] M. Frank, T. Hahn, S. Heinemeyer, W. Hollik, H. Rzehak and G. Weiglein, JHEP **0702** (2007) 047 [arXiv:hep-ph/0611326]. S. Heinemeyer, W. Hollik and G. Weiglein, Eur. Phys. J. C **9** (1999) 343 [arXiv:hep-ph/9812472]. S. Heinemeyer, W. Hollik and G. Weiglein, Comput. Phys. Commun. **124** (2000) 76 [arXiv:hep-ph/9812320].

[19] B. C. Allanach *et al.*, in *Proc. of the APS/DPF/DPB Summer Study on the Future of Particle Physics (Snowmass 2001)* ed. N. Graf, Eur. Phys. J. C **25** (2002) 113 [arXiv:hep-ph/0202233].

Alignment of the ATLAS Inner Detector tracking system

Thomas Loddenkoetter for the ATLAS Collaboration

Physikalisches Institut, Nuallee 12, 53115 Bonn, Germany

DOI: http://dx.doi.org/10.3204/DESY-PROC-2010-01/loddenkoetter

Modern tracking systems like the ATLAS Inner Detector (ID) have intrinsic resolutions that by far exceed the assembly precision. For an accurate description of the real geometry one has to obtain corrections to the nominal positions. This alignment task is crucial for efficient track reconstruction as well as for precise momentum measurement and vertex reconstruction.

The criteria for the required alignment precision at ATLAS are that the resolutions of the track parameters should not decrease by more than 20% due to alignment effects and that the systematic error on the W mass should be below < 15 MeV [1].

The ID [1][2] consists of three sub-components: the Pixel Detector (Pixel), the Semi-Conductor Tracker (SCT) and the Transition Radiation Tracker (TRT). The Pixel is a silicon pixel detector consisting of three cylindrical barrel layers and three disks in each end-cap. Its intrinsic resolution is $10 \times 115\ \mu m^2$ ($R\phi \times z$), leading to a required alignment precision of $7 \times 100\ \mu m^2$.

The SCT is a silicon strip detector with four barrel layers and nine disks per end-cap. The intrinsic resolution of the SCT is $17 \times 580\ \mu m^2$ ($R\phi \times z$), the target precision for alignment is $12 \times 200\ \mu m^2$. Pixel and SCT together consist of about 5800 modules in total.

The TRT consists of straw-like polyamide drift tubes with a diameter of 4 mm. The barrel is divided into three rings of 32 modules each, containing in total 73 layers of straws. Each end-cap consists of 160 disks of radially oriented straws. The TRT has an intrinsic resolution of 130 µm ($R\phi$ only), the target alignment precision is 30 µm.

To achieve the alignment goals, various tools are available. Already during the detector installation, *assembly and survey measurements* were performed, yielding a precision of up to O(100 µm). These measurements serve as a starting point or external constraint for other methods [3].

The SCT is equipped with a *Frequency Scanning Interferometry (FSI)* [4] system that measures deformations of the SCT with an extremely high precision of O(1 µm). Its purpose is to monitor the stability of the alignment with time. The FSI is not fully integrated in the alignment software yet.

The tool for ultimate alignment precision is *track-based alignment* which uses particle tracks to determine the alignment by examining residuals between the reconstructed hits in the detector and the intercept of the track trajectory in the module, estimated by the track fit. Several million high-p_T tracks are needed in order to reach the desired precision.

The algorithms used by ATLAS are based on minimizing the track χ^2 or on centering residual distributions by examining their mean values.

The alignment can be performed at different levels of granularity. This *alignment level* defines the "alignable structures" i.e. the substructures of the ID to which individual alignment constants are assigned. Each alignable structure has six degrees of freedom (dof), corresponding to six alignment parameters (three translations and three orientations). For the ID alignment, several alignment levels are implemented: Level 1 treats the whole Pixel as well as SCT and TRT barrel and end-caps as alignable structures, which makes 42 dof, on level 2 all ID subcomponents are split up into their barrel layers/modules and end-cap disks/layers (1146 dof). Finally, on level 3, all single sensors are aligned individually (Pixel and SCT only, about 36000 dof). Furthermore, several intermediate levels are defined that all follow the assembly structures of the detectors. For a full ID alignment, the alignment chain is run iteratively at different levels.

The baseline algorithm for track-based alignment at ATLAS is the Global χ^2 [5]. Tracks are fitted simultaneously, minimizing a global χ^2 w.r.t. all track and alignment parameters at the same time. The χ^2 definition is given in Eq. 1, where $\mathbf{r_j}$ is the vector of residuals of a track, $\boldsymbol{\tau_j}$ and $\mathbf{a}$ denote the track and alignment parameters, respectively, and V is the covariance matrix.

$$\chi^2 = \sum_{tracks} \mathbf{r_j}^T(\boldsymbol{\tau_j}, \mathbf{a})(V^{-1})_j \mathbf{r_j}(\boldsymbol{\tau_j}, \mathbf{a}) \qquad \longrightarrow \qquad \frac{d(\chi^2)}{d(\boldsymbol{\tau_j}, \mathbf{a})} \stackrel{!}{=} 0 \tag{1}$$

For minimization, the derivatives of χ^2 w.r.t. all $\boldsymbol{\tau_j}$ and $\mathbf{a}$ are required to be 0 at the same time. This leads to a linear system of N linear equations, represented by an N×N matrix, where N is the number of dofs. This can be solved by different techniques. At low granularity, the full diagonalization of the matrix is possible. All eigenmodes of the system and their eigenvalues are then known. At full granularity, a fast solution is more suitable and can be achieved with matrix conditioning. In this case the eigenvectors and -values are unknown. Also the statistical errors on alignment parameters cannot be calculated then.

Unfortunately, the χ^2 minimization is normally not sufficient for a proper alignment. The reason are the *weak modes*, which are solutions of the alignment that leave the residuals (almost) invariant, but may bias the track parameters and therefore are a source of systematics. In the χ^2 algorithm they appear as eigenmodes with very small eigenvalues, to which the algorithm is therefore insensitive. Typically, weak modes correspond to systematic deformations of the whole detector. To deal with weak modes, various measures can be taken.

The most important is to prevent the alignment from introducing weak modes. At low granularity, when the eigenmodes are known, this can be done by cutting away those modes with the lowest eigenvalues. At high granularity, when the eigenmodes are unknown, one can apply a *soft mode cut*, i.e. constrain the system by appropriately conditioning the matrix in a way that weak modes get suppressed.

Of course, cutting away or suppressing weak modes is not enough, as the real detector may contain such deformations. Aligning these requires extra steps. As weak modes are often connected to certain track topologies, a good measure is to mix tracks with different topologies, e.g. collision tracks, cosmics and beam halos. Effectively, this reduces the number of weak modes

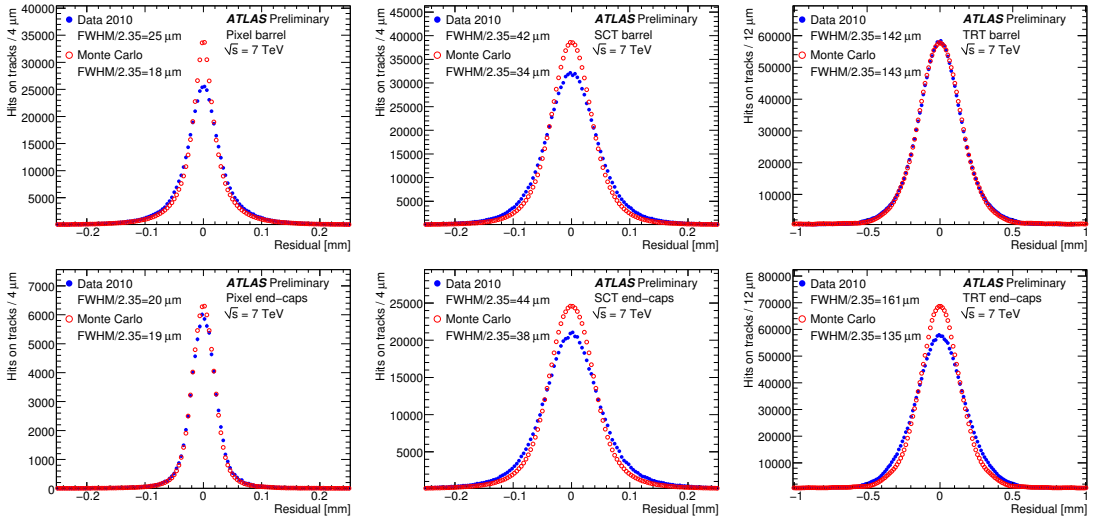

Figure 1: Unbiased residual distributions in local x coordinate for barrel and end caps of Pixel, SCT and TRT. Data points are for 7 TeV collision data from 2010 with the current alignment (dark dots) and for a simulation with perfect alignment (light circles). The simulated distributions are normalized to the number of entries in the data. The "Full Width Half-Maximum" of the distributions divided by 2.35 are quoted.

of the system. Vertex or beam spot constraints have a similar effect. Finally, one can examine quantities that *are* affected by weak modes, like invariant mass distributions of resonances etc.

Figure 1 shows the results for 7 TeV data from 2010 with the current alignment (dark dots) and for a simulation with perfect alignment (light circles). The unbiased residual distributions in the most sensitive local coordinate are presented for all sub-detectors. Tracks used for the plots were required to have $p_T > 2$ GeV and number of silicon hits ≥ 6. For these low-momentum tracks, the width of the residual distribution is larger than the intrinsic "per-hit" accuracy of the detectors due to the contribution from multiple scattering to the track parameter errors.

In the TRT end-caps the measured resolution w.r.t. the simulation is significantly worse than in the barrel. This is due to the fact that the TRT end-cap geometry did not allow for as detailed cosmic ray studies as the barrel and the Pixel and the SCT. Further commissioning of the TRT end-caps is required to achieve performance similar to that of the barrel.

References

[1] [ATLAS Collaboration], 1997, CERN-LHCC-97-16/17.

[2] G. Aad *et al.* [ATLAS Collaboration], JINST **3** (2008) S08003.

[3] T. Golling, 2006, ATL-INDET-PUB-2006-001.

[4] P. A. Coe, D. F. Howell and R. B. Nickerson, Measur. Sci. Tech. **15** (2004) 2175.
S. M. Gibson *et* al., 2005, Optics and lasers in engineering *43* 815-831

[5] P. Bruckman, A. Hicheur and S. J. Haywood, 2005, ATL-INDET-PUB-2005-002.

Forward Λ_b production in pp collisions at LHC

Gennady I. Lykasov, Denis A. Artemenkov, Vadim A. Bednyakov
JINR, Dubna, 141980, Moscow region, Russia

DOI: http://dx.doi.org/10.3204/DESY-PROC-2010-01/lykasov

As is well known, there are successful phenomenological approaches for describing the soft hadron-nucleon, hadron-nucleus and nucleus-nucleus interactions at high energies based on the Regge theory and the $1/N$ expansion in QCD, for example the quark-gluon string model (QGSM) [1] and the dual parton model (DPM) [2]. In this paper we present the results on the beauty baryon production, in particular Λ_b, in pp collisions at LHC energies and small p_t within the QGSM to find the information on the Regge trajectories of the bottom ($b\bar{b}$) mesons and the fragmentation functions (FF) of all the quarks and diquarks to this baryon. Actually, these results are the predictions for the LHC experiments.

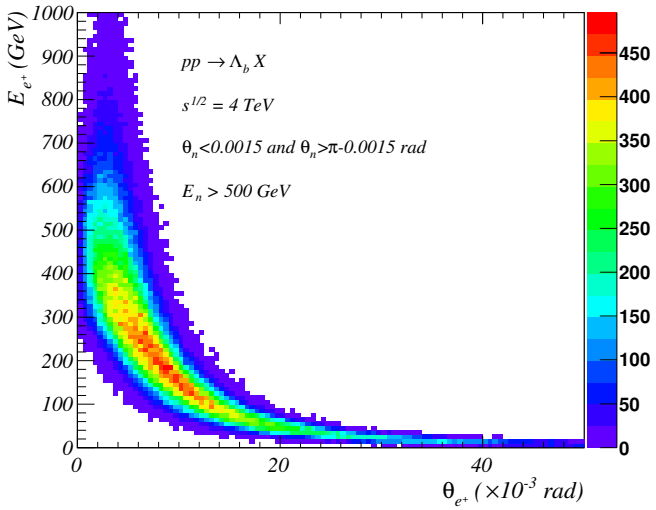

Figure 1: The distribution over θ_{e^+} and E_{e^+} in the inclusive process $pp \to \Lambda_b X \to J/\psi\,\Lambda^0 X \to e^+e^-n\,\pi^0 X$ at $\sqrt{s} = 4\,\text{GeV}$. The rate of the events is about 4.6 percent (13.8 nb).

The detailed calculations and the predictions on these reactions are presented in [3, 4], where it is shown that all the observables are very sensitive to the value of intercept $\alpha_\Upsilon(0)$ of the $\Upsilon(b\bar{b})$ Regge trajectory. The upper limit of our results is reached at $\alpha_\Upsilon(0) = 0$, when this Regge trajectory as a function of the transfer t is nonlinear. Using the hadron detector at the CMS and the TOTEM one could register the decay $\Lambda_b^0 \to J/\psi\,\Lambda^0 \to \mu^+\mu^-\pi^-p$ by detecting two muons and one proton emitted forward. However, the acceptance of the muon detector is $10^\circ \le \theta_\mu \le 170^\circ$ [5], where, according to our calculations, the fraction of these events is too low.

On the other hand, the electromagnetic calorimeter at the CMS is able to measure the dielectron pairs e^+e^- in the acceptance about $1^\circ \leq \theta_{e(e^+)} \leq 179^\circ$ [6]. Fig. 1 illustrates that the electrons and positrons produced from the J/ψ decay are emitted at very small scattering angles, mainly at $\theta_e < 16\,\text{mrad}$. The rate of these events, when the neutrons are emitted at $\theta_n < 1.5\,\text{mrad}$ and $E_n > 500\,\text{GeV}$, is about 4.6 percent (13.8 nb). In Fig. 2 the two-dimensional distribution over E_p and θ_p for the reaction $pp \to \Lambda_b X \to J/\psi\,\Lambda^0 X \to e^+e^-p\,\pi^-X$ is presented. The rate of these events is about 0.74 percent (2.22 nb). This could be reliable using the TOTEM together with the CMS [7].

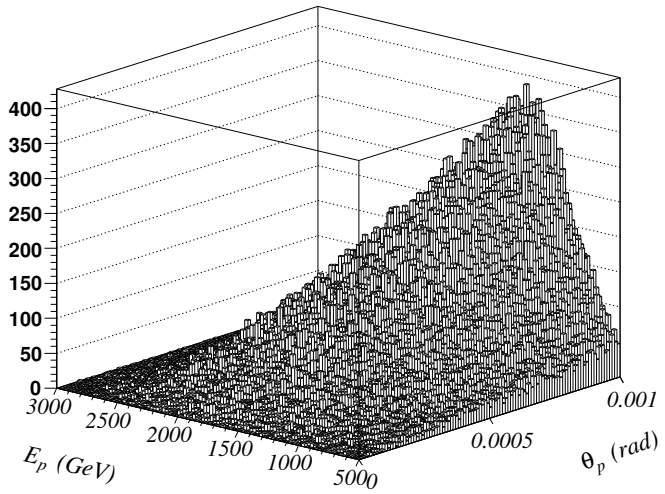

Figure 2: The two-dimensional distribution over θ_p and E_p in the inclusive process $pp \to \Lambda_b X \to J/\psi\,\Lambda^0 X \to e^+e^-p\,\pi^-X$ at $\sqrt{s} = 10\,\text{TeV}$ at $\alpha_\Upsilon(0) = 0$, when $E_p \geq 500\,\text{GeV}$ and $\theta_p \leq 1\,\text{mrad}$. The rate of these events is about 0.74 percent (2.22 nb).

The ATLAS is able also to detect e^+e^- by the electromagnetic calorimeter in the interval $1^\circ \leq \theta_{e(e^+)} \leq 179^\circ$ [5] and the neutrons emitted forward at the angles $\theta_n \leq 0.1\,\text{mrad}$ [8]. In Fig. 3 we present the prediction for the reaction $pp \to \Lambda_b X \to J/\psi\,\Lambda^0 X \to e^+e^-n\,\pi^0 X$, that could be reliable at the ATLAS experiment. The rate of these events is about 0.015 percent (45 pb).

The TOTEM [9] together with the CMS might be able to measure the channel $\Lambda_b \to J/\psi\,\Lambda^0 \to e^+e^-\pi^-p$ (the integrated cross-section is about 0.2–0.3 μb at $\alpha_\Upsilon(0) = 0$ and smaller at $\alpha_\Upsilon(0) = -8$). The T2 and T1 tracking stations of the TOTEM apparatus have their angular acceptance in the intervals $3\,\text{mrad} < \theta < 10\,\text{mrad}$ (corresponding to $6.5 > \eta > 5.3$) and $18\,\text{mrad} < \theta < 90\,\text{mrad}$ (corresponding to $4.7 > \eta > 3.1$) respectively, and could thus detect 42% of the muons from the J/ψ decay. In the same angular intervals, 36% of the π^- and 35% of the protons from the Λ^0 decay are expected. According to a very preliminary estimate [7], protons with energies above 3.4 TeV emitted at angles smaller than 0.6 mrad could be detected in the Roman Pot station at 147 m from IP5 [9, 7]. In the latter case, the reconstruction of the proton kinematics may be possible, whereas the trackers T1 and T2 do not provide any momentum or energy information. Future detailed studies are to establish the full event topologies with all correlations between the observables in order to assess whether the signal events can be identified and separated from backgrounds. These investigations should also

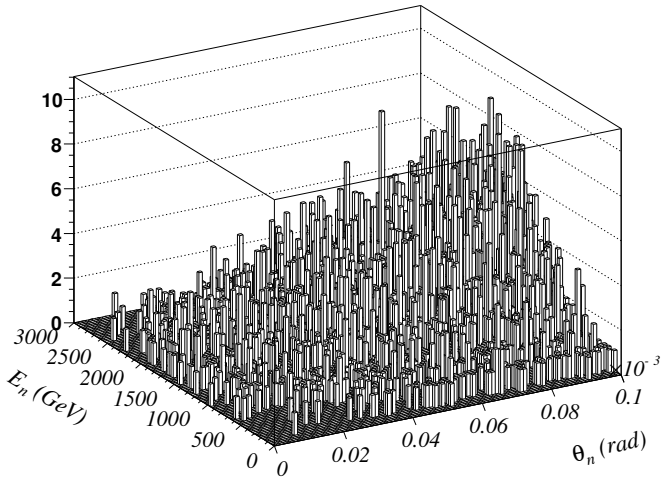

Figure 3: The two-dimensional distribution over θ_p and E_p in the inclusive process $pp \to \Lambda_b X \to J/\psi\,\Lambda^0 X \to e^+e^- n\,\pi^0 X$ at $\sqrt{s} = 10\,\text{TeV}$ at $\alpha_\Upsilon(0) = 0$, when $\theta_p \leq 0.1\,\text{mrad}$. The rate of these events is about 0.015 percent (45 pb).

include the CMS calorimeters HF and CASTOR which cover the same angular ranges as T1 and T2 respectively [7].

Acknowledgments

We are very grateful to V. V. Lyubushkin for a help in the MC calculations. We also thank M. Deile, P. Grafström, and N. I. Zimin for extremely useful help related to the possible experimental check of the suggested predictions at the LHC and the preparation of this paper. We are also grateful to D. Denegri, K. Eggert, A. B. Kaidalov, and M. Poghosyan for very useful discussions. This work was supported in part by the Russian Foundation for Basic Research grant N: 08-02-01003.

References

[1] A. B. Kaidalov and K. A. Ter-Martirosyan, Phys. Lett. B **116** (1982) 489, [arXiv:hep-ph/0909.5061].

[2] A. Capella, U. Sukhatme, C. I. Tan and J. Tran Than Van Phys. Rep. **236** (1994) 225, [arXiv:hep-ph/0909.5061].

[3] G. I. Lykasov, V. V. Lyubushkin and V. A. Bednyakov, Nucl. Phys. [Proc. Suppl.] **198** (2010) 165 [arXiv:hep-ph/0909.5061].

[4] V. A. Bednyakov, G. I. Lykasov and V. V. Lyubushkin, arXiv:hep-ph/1005.0559.

[5] ATLAS Collaboration, Technical Design Report, ATLAS-TDR-017,CERN-LHCC-2005-022.

[6] CMS Collaboration J. Phys. G: Nucl. Part. Phys. **34** (2007) 995.

[7] M. Deile, Private communication; H. Niewiadomski, TOTEM-NOTE, **002** (2009).

[8] ATLAS Collaboration, Letter of Intent "Zero Degree Calorimeters".

[9] TOTEM Collaboration, Technical Design Report, (2004),CERN-LHCC-2004-002; Addendum CERN-LHCC-2004-020, "The Totem Experiment At The CERN Large Hadron Collider", JINST **3**2008 S08007.

On the phenomenology of a two-Higgs-doublet model with maximal CP symmetry at the LHC – synopsis and addendum

M. Maniatis[1], *A. von Manteuffel*[2], *O. Nachtmann*[1]

[1]Institut für Theoretische Physik, Universität Heidelberg, Philosophenweg 16, 69120 Heidelberg, Germany
[2]Institut für Theoretische Physik, Universität Zürich, Winterthurerstr. 190, 8057 Zürich, Switzerland

DOI: http://dx.doi.org/10.3204/DESY-PROC-2010-01/maniatis

Predictions for LHC physics are given for a two-Higgs-doublet model having four generalized CP symmetries. In this *maximally-CP-symmetric model* (MCPM) the first fermion family is, at tree level, uncoupled to the Higgs fields and thus massless. The second and third fermion families have a very symmetric coupling to the Higgs fields. But through the electroweak symmetry breaking a large mass hierarchy is generated between these fermion families, that is, we find roughly what is observed in Nature. In this paper we present a short outline of the model and extend a former study by the predictions at LHC for a center-of-mass energy of 7 TeV.

1 Introduction

Extending the Standard Model (SM) Higgs sector to two Higgs doublets, φ_1, φ_2, gives the two-Higgs-doublet model (THDM). Many properties of THDMs turn out to have a simple geometric meaning if we introduce gauge invariant bilinears [1, 2],

$$K_0 = \varphi_1^\dagger\varphi_1 + \varphi_2^\dagger\varphi_2, \qquad \mathbf{K} = \begin{pmatrix} K_1 \\ K_2 \\ K_3 \end{pmatrix} = \begin{pmatrix} \varphi_1^\dagger\varphi_2 + \varphi_2^\dagger\varphi_1 \\ i\varphi_2^\dagger\varphi_1 - i\varphi_1^\dagger\varphi_2 \\ \varphi_1^\dagger\varphi_1 - \varphi_2^\dagger\varphi_2 \end{pmatrix}. \tag{1}$$

In terms of these bilinears K_0, $\mathbf{K}$, the most general THDM Higgs potential reads

$$V = \xi_0 K_0 + \boldsymbol{\xi}^{\mathrm{T}}\mathbf{K} + \eta_{00}K_0^2 + 2K_0\boldsymbol{\eta}^{\mathrm{T}}\mathbf{K} + \mathbf{K}^{\mathrm{T}}E\mathbf{K} \tag{2}$$

with parameters ξ_0, η_{00}, 3-component vectors $\boldsymbol{\xi}$, $\boldsymbol{\eta}$ and a 3×3 matrix $E = E^{\mathrm{T}}$, all real.

Generalised CP transformations (GCPs) are defined by [5, 6, 7]

$$\varphi_i(x) \to U_{ij}\,\varphi_j^*(x'), \qquad i,j = 1,2\,, \qquad x' = (x^0, -\mathbf{x}) \tag{3}$$

with U an arbitrary unitary 2×2 matrix and $U = \mathbb{1}_2$ corresponds to the standard CP transformation. In terms of the bilinears this reads [3, 4]

$$K_0(x) \to K_0(x'), \qquad \mathbf{K}(x) \to \bar{R}\,\mathbf{K}(x') \tag{4}$$

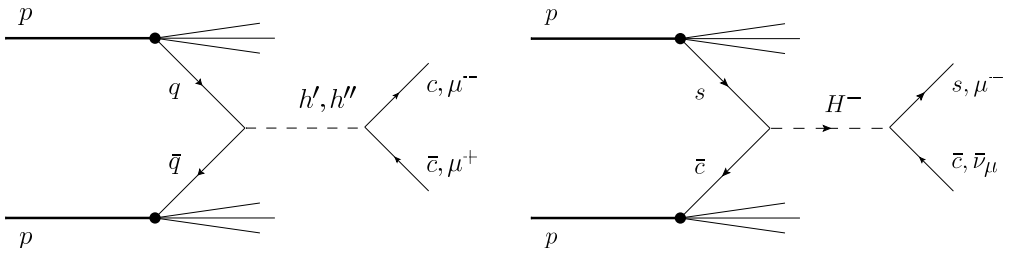

Figure 1: Feynman diagrams for the Drell–Yan type Higgs-boson production and decay reactions which are enhanced in the MCPM ($q = c, s$).

with an improper rotation matrix $\bar{R}$. Requiring $\bar{R}^2 = \mathbb{1}_3$ leads to two types of GCPs. In K space: (i) $\bar{R} = -\mathbb{1}_3$, point reflection, (ii) $\bar{R} = R^{\mathrm{T}}\, \bar{R}_2\, R$, reflection on a plane ($R \in SO(3)$), where $\bar{R}_2 = \mathrm{diag}(1, -1, 1)$ is in K space a reflection on the 1–3 plane.

While the CP transformations of type (ii) are equivalent to the standard CP transformation, the point reflection transformation of type (i) is quite different and turns out to have very interesting properties. Motivated by this geometric picture of generalised CP transformations, the most general THDM invariant under the point reflection (i) has been studied in [8, 9, 10]. The corresponding potential has to obey the conditions $\boldsymbol{\xi} = \boldsymbol{\eta} = 0$,

$$V_{\mathrm{MCPM}} = \xi_0\, K_0 + \eta_{00}\, K_0^2 + \mathbf{K}^{\mathrm{T}}\, E\, \mathbf{K}\,. \tag{5}$$

This model is, besides the point reflection symmetry of type (i), invariant under three GCPs of type (ii). We call this model therefore maximally CP symmetric model, MCPM. Requiring also maximally CP symmetric Yukawa couplings we find that at least two fermion families are necessary in order to have non-vanishing fermion masses. That is, we find a reason for family replication in the MCPM. Furthermore, requiring absence of large flavor changing neutral currents it was shown that the Yukawa couplings are completely fixed. For instance for the lepton sector we get the Yukawa couplings

$$\mathscr{L}_{\mathrm{Yuk}} = -\sqrt{2}\frac{m_\tau}{v}\left\{\bar{\tau}_R\, \varphi_1^\dagger \begin{pmatrix}\nu_\tau \\ \tau\end{pmatrix}_L - \bar{\mu}_R\, \varphi_2^\dagger \begin{pmatrix}\nu_\mu \\ \mu\end{pmatrix}_L\right\} + h.c. \tag{6}$$

The physical Higgs-boson fields are denoted by ρ', h', h'', and $H^\pm$.

Let us briefly summarize the essential properties of the MCPM: There are 5 physical Higgs particles, three neutral ones, ρ', h', h'', and a charged Higgs-boson pair $H^\pm$. Under the standard CP transformation, ρ' and h' are even, while h'' is odd. The ρ' boson couples exclusively to the third (τ, t, b) family, ρ' behaves like the SM Higgs boson. The Higgs bosons h', h'', $H^\pm$ couple exclusively to the second (μ, c, s) family with strengths proportional to the masses of the third generation fermions. The first (e, u, d) family is uncoupled to the Higgs bosons. For further details we refer to [8].

2 Predictions for hadron colliders

Since the Yukawa couplings of the h', h'', $H^\pm$ Higgs bosons to the second fermion family are proportional to the third-fermion-family masses we have large cross sections for Drell–Yan type

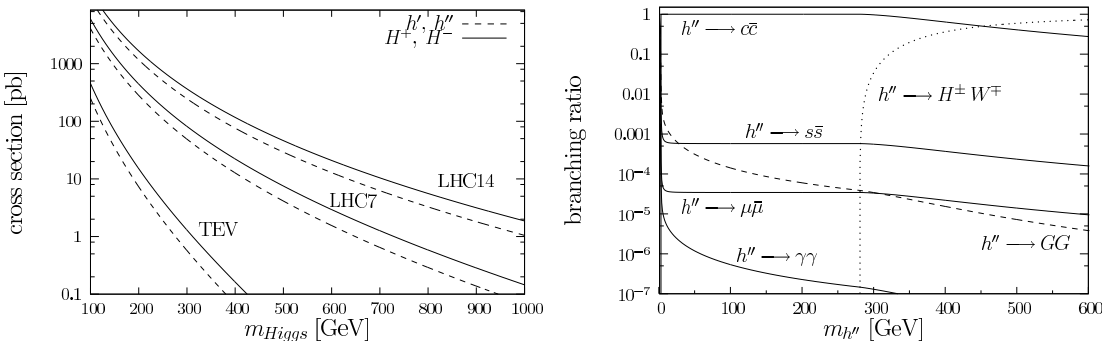

Figure 2: left: total cross section of Drell–Yan type Higgs boson production at TEVATRON and LHC. right: branching ratios of the CP odd h'' Higgs boson, where a mass of $m_{H^\pm} = 200$ GeV is assumed.

Higgs-boson production, that is, Higgs-boson production in quark–antiquark annihilation. For the same reason we have large decay rates of these Higgs bosons to the second generation fermions. In Figure 1 we show the diagrams for these production and decay reactions in pp collisions. In [9] the cross sections were computed for Drell-Yan Higgs-boson production at the TEVATRON and the LHC for center-of-mass energies of 1.96 TeV and 14 TeV, respectively. In [10] radiative effects were considered. Here we add the cross sections for a center-of-mass energy of 7 TeV at LHC, which is currently available. The corresponding total cross sections for the Drell–Yan production of the h', h'', $H^\pm$ bosons are shown in Figure 2. In this figure we also recall the branching ratios of the h'' boson decays. As an example consider Higgs-boson masses h', h'', $H^\pm$ of 200 GeV where we get very large total production cross sections, around 850 pb, for LHC7. These Higgs bosons decay mainly into light c and s quarks. However, tagging of c and s-quarks in the detectors is at least challenging. Channels involving muons should be more easily accessible experimentally. With the branching ratio of 3×10^{-5} into μ-pairs, we predict about 25 μ events from a 200 GeV h' (h'') at LHC7 for 1 fb^{-1} integrated luminosity. For further details of the calculations we refer to [8, 9, 10].

References

[1] F. Nagel, PhD thesis, Heidelberg (2004) `http://www.slac.stanford.edu/spires/find/hep/www?irn=6461018`.

[2] M. Maniatis, A. von Manteuffel, O. Nachtmann and F. Nagel, Eur. Phys. J. C **48**, 805 (2006)

[3] C. C. Nishi, Phys. Rev. D **74** 036003 (2006)

[4] M. Maniatis, A. von Manteuffel and O. Nachtmann, Eur. Phys. J. C **57** (2008) 719

[5] T. D. Lee and G. C. Wick, Phys. Rev. **148**, 1385 (1966).

[6] G. Ecker, W. Grimus and W. Konetschny, Nucl. Phys. B **191** (1981) 465,

[7] G. Ecker, W. Grimus and H. Neufeld, Nucl. Phys. B **247** (1984) 70,

[8] M. Maniatis, A. von Manteuffel and O. Nachtmann, Eur. Phys. J. C **57** (2008) 739

[9] M. Maniatis and O. Nachtmann, JHEP **05** (2009) 028

[10] M. Maniatis and O. Nachtmann, JHEP **04** (2010) 027

Performance of the ATLAS liquid argon calorimeter

Zhaoxia Meng on behalf of the ATLAS Liquid Argon Calorimeter Group

Institute of Physics, Academia Sinica, TW-Taipei 11529, Taiwan.
Also at School of Physics, Shandong University, Jinan, P.R.China.

DOI: http://dx.doi.org/10.3204/DESY-PROC-2010-01/meng

The liquid argon calorimeter (LAr) [1] of the ATLAS detector [2] measures energy deposited by particles produced in p-p collisions at the CERN Large Hadron Collider (LHC). Figure 1 illustrates the LAr system. It consists of the electromagnetic calorimeter (EM), the hadronic end-cap (HEC) and the forward calorimeter (FCAL). The material utilized for collecting signal is liquid argon. The absorber consists of lead in the EM, copper in the HEC and the first layer of the FCAL and tungsten alloy in the outer two layers of the FCAL. Copper electrodes, electronic boards and various support structures constitute additional material in the calorimeter.

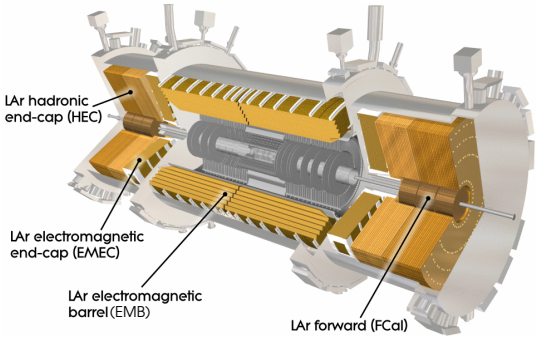

Figure 1: Schematic view of the liquid argon calorimeter system.

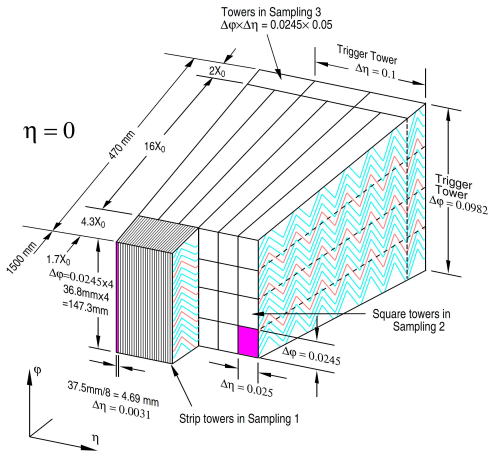

Figure 2: Readout granularity of the EM calorimeter.

The LAr is a sampling calorimeter with fine granularity, especially in the first EM layer, large coverage in $|\eta|$, up to $|\eta| = 4.9$, and full coverage in ϕ. Figure 2 illustrates the granularity of the EM calorimeter [3]. The design energy resolutions for each LAr sub-detector are listed in Table 1.

Ionization electrons are produced by passage of charged particles. They drift to electrodes and produce electrical currents proportional to the energy deposited. The currents have triangular shapes that are amplified, shaped and then sampled $N_{samples}$ (default is 5) times every 25 ns. Each sample is then digitized. The triangular signal has a $\sim$1 ns rise time and several

hundreds ns decay time (T_{drift}). The drift time in the barrel region of the calorimeter has a constant value ∼460 ns. Smaller values in the end-caps reflect gap width decreasing with $|\eta|$ [4].

The ionization signal shape can be predicted by modeling of the electronic readout chain. The ionization signal shape is predicted by describing the signal propagation and the response of the electronic readout, that are determined or tuned by the calibration system [4]. A calibration pulse of precisely known amplitude is injected into each cell through the same path as seen through the ionization pulse so probing the electrical and readout properties of each cell. Figure 3 illustrates the agreement of the measured signal shape and the predicted one. The difference is less than 4% [5].

	Resolution
EM Barrel	$\frac{\sigma_E}{E} = \frac{10\%}{\sqrt{E}} \bigoplus 0.7\%$
EM End-Cap	$\frac{\sigma_E}{E} = \frac{10\%}{\sqrt{E}} \bigoplus 0.7\%$
HEC	$\frac{\sigma_E}{E} = \frac{50\%}{\sqrt{E}} \bigoplus 3\%$
FCAL	$\frac{\sigma_E}{E} = \frac{100\%}{\sqrt{E}} \bigoplus 10\%$

Table 1: Design energy resolutions of the LAr calorimeters.

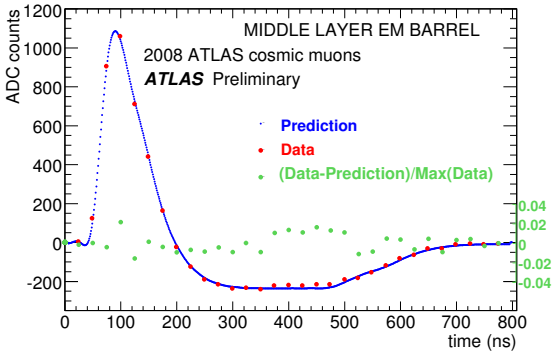

Figure 3: Typical ionization pulse shape in the EM barrel.

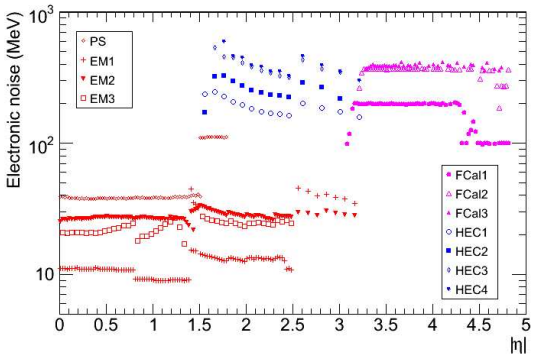

Figure 4: Electronic noise at cell level as a function of $|\eta|$ for each longitudinal layer of the calorimeter.

The individual cell energy is reconstructed from the digitized signal according to the formula:

$$E_{cell} = F_{\mu A \to MeV} \times F_{DAC \to \mu A} \times \left(\frac{M_{phys}}{M_{cali}}\right)^{-1} \times G \times A\,, \tag{1}$$

where A is the amplitude in ADC counts, G represents the gain, $\frac{M_{phys}}{M_{cali}}$ is a correction for the difference of the maxima between the injected and the ionization pulses, $F_{DAC \to \mu A}$ converts current in DAC units to μA and $F_{\mu A \to MeV}$ converts current to energy.

Pedestal, gains and noise are parameters used in the energy reconstruction. Their determination is very important since they affect signal to background ratio and energy resolution.

Pedestal is obtained from runs taken without any beam or calibration pulse injection. Average pedestal is computed for each cell in every run. Gains are obtained from calibration runs. In these runs, a set of fixed current DAC is injected into each cell N times, in which M≤N events are triggered, sampled and digitized. Average response of the M events for each sample is calculated and used to reconstruct the maximum amplitude of the pulse. Gains are obtained by fitting the maximum amplitude as a function of DAC. Stability of the pedestal and gain

studied during 6 months in 2009 shows good results. The largest variation of pedestal is 10 MeV from the medium gain in the FCAL. The relative variation of the gain is within 0.3% [5].

Electronic noise (σ_{noise}) as a function of η obtained from randomly triggered events is shown in Figure 4. The noise ranges from 10 to 50 MeV in the EM calorimeter, and from 100 to 500 MeV in the HEC and the FCAL where the size of cells is much larger than that in the EM calorimeter.

The readout clock of each LAr cell must be synchronized to the LHC bunch crossing in order to reconstruct correct energy for every event. Alignment of timing-in for all the LAr cells within 1 ns is required. Measurements of the timing alignment performed in different data taking periods show that the LAr cells are in time as required.

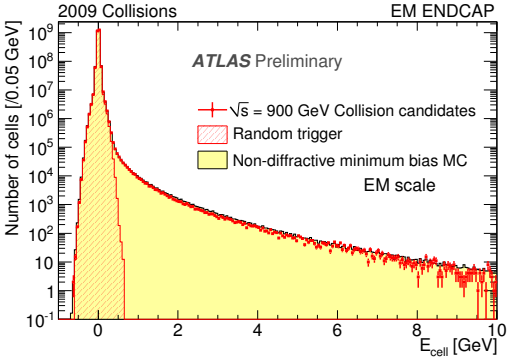

Figure 5: Cell energy distribution for collision events in the EM end-cap calorimeter.

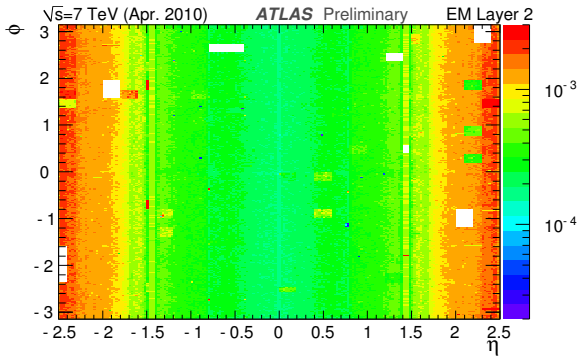

Figure 6: Cell occupancy map in the EM calorimeter with 7 TeV collision data.

Since the delivery of collision data started in 2009, various performance studies have been done. Figure 5 illustrates the cell energy distributions in the EM end-caps. Random trigger events record mainly cell noise. Good agreement between the data and simulated signal due to collision events is observed. Figure 6 illustrates the occupancy map for the second layer of the EM calorimeter. Cell energy larger than 5 σ_{noise} is plotted. White rectangles correspond to the ∼1.3% dead readout channels [5].

In addition to the studies of LAr performance discussed above, the temperature uniformity and contamination of the liquid argon were also checked. The measured values are all consistent with design. No extra contribution has been found to global resolution constant term [5].

References

[1] ATLAS liquid argon calorimeter: Technical design report, The ATLAS Collaboration, CERN-LHCC-96-41 (1996) [http://cdsweb.cern.ch/record/331061?ln=pt]

[2] G Aad et al, "The ATLAS Experiment at the CERN Large Hadron Collider, The ATLAS Collaboration" JINST 3 (2008) S08003 [http://cdsweb.cern.ch/record/1125884]

[3] Calorimeter Performance Technical Design Report, The ATLAS Collaboration [http://atlas.web.cern.ch/Atlas/TDR/caloperf/caloperf.html]

[4] G.Aad et al., Drift Time Measurement in the ATLAS Liquid Argon Electromagnetic Calorimeter using Cosmic Muons, The ATLAS Collaboration, Accepted by EPJC [http://arxiv.org/abs/1002.4189]

[5] G.Aad et al., Readiness of the ATLAS Liquid Argon Calorimeter for LHC Collisions, The ATLAS Collaboration, Accepted by EPJC [http://arxiv.org/abs/0912.2642]

Neutral MSSM Higgs and Z boson associated production at the LHC

Caesar P. Palisoc[1], *Bernd A. Kniehl*[2]

[1]National Institute of Physics, University of the Philippines, Diliman, Queson City 1101, Philippines
[2]II. Institut für Theoretische Physik, Universität Hamburg, Luruper Chaussee 149, 22761 Hamburg, Germany

DOI: http://dx.doi.org/10.3204/DESY-PROC-2010-01/palisoc

We study the associated hadroproduction of a neutral Higgs and a Z Boson within the minimal supersymmetric standard model (MSSM). We calculate the partonic cross sections for producing CP-odd neutral Higgs boson plus Z boson analytically to lowest order. To LO, the contributing partonic cross sections include tree-level quark-antiquark ($q\overline{q}$) annihilation and one-loop gluon-gluon (gg) fusion, which proceeds via quark and squark loops. The cross sections are expressed in terms of helicity amplitudes. We present cross sections as functions of the Higgs mass and $\tan\beta$ assuming LHC experimental conditions.

We focus on the hadronic production of a neutral CP-odd MSSM Higgs boson in association with a Z boson. We describe and list the lowest order contribution to the hadronic production cross section and explore the phenomenological consequence under experimental conditions of the LHC.

We present the LO cross sections of the partonic subprocesses $q\overline{q} \to ZA^0$ and $gg \to ZA^0$ in the MSSM. We work in the parton model of QCD with $n_f = 5$ active quark flavors $q = u, d, s, c, b$, which we take to be massless. However, we retain the b-quark Yukawa couplings at their finite values, in order not to suppress possibly sizeable contributions. The various couplings v_{Zqq}, a_{Zqq}, $g_{\phi qq}$, $g_{h^0A^0Z}$, $g_{H^0A^0Z}$, g_{h^0ZZ}, and g_{H^0ZZ} are readily available in the literature.

Considering the generic partonic subprocess $ab \to ZA^0$, we denote the four-momenta of the incoming partons, a and b, and the outgoing Z and A^0 bosons by p_a, p_b, p_Z, and p_{A^0}, respectively, and define the partonic Mandelstam variables as $s = (p_a + p_b)^2$, $t = (p_a - p_Z)^2$, and $u = (p_b - p_Z)^2$. The on-shell conditions read $p_a^2 = p_b^2 = 0$, $p_Z^2 = m_Z^2 = z$, and $p_{A^0}^2 = m_{A^0}^2 = h$. Four-momentum coservation implies that $s + t + u = z + h$. Furthermore, we have $sp_T^2 = tu - zh = N$, where p_T is the absolute value of transverse momentum common to the Z and A^0 bosons in the center-of-mass (c.m.) frame.

The differential cross section for the tree-level $b\overline{b}$ annihilation may be generically written as

$$\begin{aligned}\frac{d\sigma}{dt}\left(b\bar{b} \to ZA^0\right) &= \frac{G_F^2 c_w^4 z}{3\pi s}\left[\lambda|S|^2 - 4sp_T^2\left(\frac{1}{t}+\frac{1}{u}\right)g_{A^0bb}a_{Zbb}\Re S\right.\\ &\left. + g_{A^0bb}^2\left(v_{Zbb}^2 T_+ + a_{Zbb}^2 T_-\right)\right], \qquad (1)\end{aligned}$$

where G_F is the Fermi constant, $\lambda = s^2+z^2+h^2-2(sz+zh+hs)$, and $S = g_{h^0A^0Z}g_{h^0bb}\mathcal{P}_{h^0}(s)+$

$g_{H^0A^0Z}g_{H^0bb}\mathcal{P}_{H^0}(s)$, $T_\pm = 2 \pm 2 + 2p_T^2\left[z\left(\frac{1}{t}\pm\frac{1}{u}\right)\mp\frac{2s}{tu}\right]$. Here, $\mathcal{P}_X(s) = \frac{1}{s-m_X^2+im_X\Gamma_X}$ is the propagator function of particle X, with mass m_X and total decay width Γ_X.

We express the quark and squark one-loop contributions to the gg fusion in terms of helicity amplitudes. We label the helicity states of the two gluons and the Z boson in the partonic c.m. frame by $\lambda_a = -1/2, 1/2, \lambda_b = -1/2, 1/2$, and $\lambda_Z = -1, 0, 1$. The helicity amplitudes of the quark and squark triangle contributions read

$$\begin{aligned}
\mathcal{M}^{\triangle}_{\lambda_a\lambda_b 0} &= 8i\sqrt{\frac{\lambda}{z}}(1+\lambda_a/\lambda_b)\sum_q m_q\left(g_{h^0A^0Z}g_{h^0qq}\mathcal{P}_{h^0}(s)+g_{H^0A^0Z}g_{H^0qq}\mathcal{P}_{H^0}(s)\right)F_\triangle\left(s,m_q^2\right),\\
\tilde{\mathcal{M}}^{\triangle}_{\lambda_a\lambda_b 0} &= -2i\sqrt{\frac{\lambda}{z}}(1+\lambda_a/\lambda_b)\sum_{\tilde{q}_i}\left(g_{h^0A^0Z}g_{h^0\tilde{q}_i\tilde{q}_i}\mathcal{P}_{h^0}(s)+g_{H^0A^0Z}g_{H^0\tilde{q}_i\tilde{q}_i}\mathcal{P}_{H^0}(s)\right)\tilde{F}_\triangle\left(s,m_{\tilde{q}_i}^2\right).
\end{aligned}$$

where $F_\triangle(s,m_q^2) = 2+(4m_q^2-s)C^{00}_{qqq}(s)$, and $\tilde{F}_\triangle(s,m_{\tilde{q}_i}^2) = 2+4m_{\tilde{q}_i}^2C^{00}_{\tilde{q}_i\tilde{q}_i\tilde{q}_i}(s)$ are the quark and squark triangle form factors, respectively, and $C^{00}_{qqq}(s) = C_0(0,0,m_q^2,m_q^2,m_q^2)$ is the scalar three-point function. As for the quark box contribution, all twelve helicity combinations contribute. Due to Bose symmetry, they are related by $\mathcal{M}^{\square}_{\lambda_a\lambda_b\lambda_Z}(t,u) = (-1)^{\lambda_Z}\mathcal{M}^{\square}_{\lambda_b\lambda_a\lambda_Z}(u,t)$, $\mathcal{M}^{\square}_{\lambda_a\lambda_b\lambda_Z}(t,u) = \mathcal{M}^{\square}_{-\lambda_a-\lambda_b-\lambda_Z}(t,u)$. Keeping $\lambda_Z = \pm1$ generic, we thus only need to specify four expressions. These read

$$\begin{aligned}
\mathcal{M}^{\square}_{++0} &= -\frac{8i}{\sqrt{z\lambda}}\sum_q g_{A^0qq}a_{Zqq}m_q\left[F^0_{++}+(t\leftrightarrow u)\right],\\
\mathcal{M}^{\square}_{+-0} &= -\frac{8i}{\sqrt{z\lambda}}\sum_q g_{A^0qq}a_{Zqq}m_q\left[F^0_{+-}+(t\leftrightarrow u)\right],\\
\mathcal{M}^{\square}_{++\lambda_Z} &= -4i\sqrt{\frac{2N}{s}}\sum_q g_{A^0qq}a_{Zqq}m_q\left[F^1_{++}-(t\leftrightarrow u)\right],\\
\mathcal{M}^{\square}_{+-\lambda_Z} &= -4i\sqrt{\frac{2N}{s}}\sum_q g_{A^0qq}a_{Zqq}m_q\left[F^1_{+-}-(t\leftrightarrow u,\lambda_Z\to-\lambda_Z)\right].
\end{aligned}\tag{2}$$

The quark box form factors, $F^{|\lambda_Z|}_{\lambda_a\lambda_b}$, are functions of s,t,u, and depend on the scalar three- and four-point function. They are quite lengthy to be included here. We recall that $\tilde{\mathcal{M}}_{\lambda_a\lambda_b\lambda_Z} = 0$.

The differential cross section of $gg\to ZA^0$ is then given by

$$\frac{d\sigma}{dt}(gg\to ZA^0) = \frac{\alpha_s^2(\mu_r)G_F^2m_W^4}{256(4\pi)^3s^2}\sum_{\lambda_a,\lambda_b,\lambda_Z}\left|\mathcal{M}^{\triangle}_{\lambda_a\lambda_b\lambda_Z}+\mathcal{M}^{\square}_{\lambda_a\lambda_b\lambda_Z}+\tilde{\mathcal{M}}^{\triangle}_{\lambda_a\lambda_b\lambda_Z}\right|^2,\tag{3}$$

where $\alpha_s(\mu_r)$ is the strong-coupling constant at renormalization scale μ_r. Due to Bose symmetry, the right-hand side of Eq. (3) is symmetric in t and u.

We are now in a position to explore the phenomenological implications of our results. The SM input parameters for our numerical analysis are taken to be $G_F = 1.16637\times10^{-5}$ GeV^{-2}, $m_W = 80.398$ GeV, $m_Z = 91.1876$ GeV, $m_t = 171.3$ GeV , and $\overline{m}_b(\overline{m}_b) = 4.20$ GeV [1]. We adopt the LO proton PDF set CTEQ6L1 [2]. We evaluate $\alpha_s(\mu_r)$ and $m_b(\mu_r)$ from the LO formulas, which may be found, *e.g.*, in Eqs. (23) and (24) of Ref. [3], respectively, with $n_f = 5$ quark flavors and asymptotic scale parameter $\Lambda^{(5)}_{QCD} = 165$ MeV [2]. We identify the

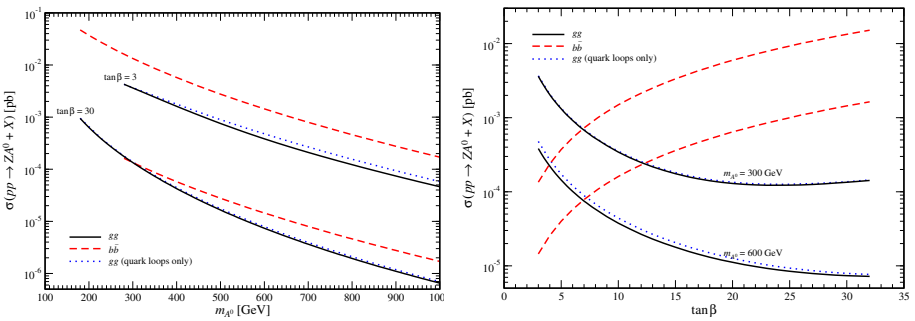

Figure 1: Total cross sections σ (in fb) of the $p\overline{p} \to ZA^0 + X$ via $b\overline{b}$ annihilation (dashed lines) and gg fusion (solid lines) at the LHC as functions of m_{A^0} for $\tan\beta = 3$ and 30, and as functions of $\tan\beta$ for $m_{A^0} = 300$ GeV and 600 GeV. The dotted lines correspond to gg fusion originating from quark loops only.

renormalization and factorization scales with the $Z\phi$ invariant mass $\sqrt{s}$. We vary $\tan\beta$ and m_{A^0} in the ranges $3 < \tan\beta < 32 \approx m_t/m_b$ and 180 GeV $< m_{A^0} <$ 1 TeV, respectively. As for the GUT parameters, we choose $m_{1/2} = 150$ GeV, $A = 0$, and $\mu < 0$, and tune m_0 so as to be consistent with the desired value of m_{A^0}. All other MSSM parameters are then determined according to the SUGRA-inspired scenario as implemented in the program package SUSPECT [4]. We do not impose the unification of the τ-lepton and b-quark Yukawa couplings at the GUT scale, which would just constrain the allowed $\tan\beta$ range without any visible effect on the results for these values of $\tan\beta$. We exclude solutions which do not comply with the present experimental lower mass bounds of the sfermions, charginos, neutralinos, and Higgs bosons [1].

Figure 1 shows the fully integrated cross sections of $pp \to ZA^0 + X$ at the LHC as functions of m_{A^0} for $\tan\beta = 3$ and 30, and as functions of $\tan\beta$ for $m_{A^0} = 300$ GeV and 600 GeV, with c.m. energy $\sqrt{S} = 14$ TeV. We note that the SUGRA-inspired MSSM with our choice of input parameters does not permit $\tan\beta$ and m_{A^0} to be simultaneously small, due to the experimental lower bound on the selectron mass [1]. This explains why the curves for $\tan\beta = 3$ only start at $m_{A^0} \approx 280$ GeV, while those for $\tan\beta = 30$ already start at $m_{A^0} \approx 180$ GeV. The $b\overline{b}$-annihilation contribution (dashed lines), which originates from the Yukawa-enhanced amplitudes, and the total gg-fusion contributions (solid lines), corresponding to the coherent superposition of quark and squark loop amplitudes, are given separately. It shows that the $b\overline{b}$-annihilation dominates at large to moderate values of $\tan\beta$. On the other hand, the gg-fusion dominates at small values of $\tan\beta$. We note further that the squark loop contribution, although minimal, tend to decrease the total gg-fusion contribution.

References

[1] Particle Data Group, C. Amsler *et al.*, Phys. Lett. B **667**, 1 (2008).

[2] J. Pumplin, D. R. Stump, J. Huston, H.-L. Lai, P. Nadolsky, and W.-K. Tung, JHEP **0207**, 012 (2002) [arXiv:hep-ph/0201195].

[3] B. A. Kniehl, Z. Phys. C **72**, 437 (1996) [arXiv:hep-ph/9403386].

[4] A. Djouadi, J. L. Kneur, and G. Moultaka, Comput. Phys. Commun. **176**, 426 (2007) [arXiv:hep-ph/0211331].

Performance of the ATLAS inner detector trigger algorithms in p-p collisions at $\sqrt{s} = 900$ GeV and $\sqrt{s} = 7$ TeV

Andrea Ferretto Parodi for the ATLAS Collaboration

DESY, Notkestraße 85, 22607 Hamburg, Germany

DOI: http://dx.doi.org/10.3204/DESY-PROC-2010-01/ferrettoparodi

The ATLAS inner detector trigger algorithms have been running online during data taking with proton-proton collisions at the Large Hadron Collider (LHC) in December 2009 and spring 2010 at the centre-of-mass energies of 900 GeV and 7 TeV.

The inner detector [1] is the ATLAS subdetector closest to the interaction point and provides precise tracking and momentum measurement of particles created in the collisions. It is composed of the pixel detector (silicon pixels), the semiconductor tracker (SCT, silicon stereo strips) and the transition radiation tracker (TRT, straw drift tubes). The whole detector is immersed in a 2 T solenoid magnetic field.

The ATLAS trigger [1], designed to reject uninteresting collision events in real time, performs the online event selection in three stages, called Level-1 (L1), Level-2 (L2) and event filter (EF). L1 is hardware based and has access to summary event informations from the calorimeters and the muon spectrometer, and defines one or more regions of interest (RoIs), geometrical regions of the detector, identified by η and ϕ coordinates, containing interesting physics objects. L2 and the EF (globally called high level trigger, HLT) are software based and can access information from all subdetectors, including the inner detector. RoI based reconstruction reduces the data access (to $\sim 2\%$ of the entire event) and also the processing time by performing the reconstruction only in the region relevant for the trigger decision. Globally, the ATLAS trigger reduces the acquisition rate to about 200 Hz, down from a proton-proton bunch crossing rate of 40 MHz.

HLT tracking algorithms run on a farm of commercial CPUs, and their basic task is to reconstruct trajectories of charged particles, used for the definition of many trigger items (high p_T leptons, tracks coming from τ decays, jets or B-hadrons decays) and for the determination of the online beam spot (more details in the following). L2 is based on fast custom algorithms, while the EF is based on offline tools, adapted to take into account trigger requirements.

Performance of the HLT algorithms in terms of tracking efficiency is measured w.r.t. offline reconstructed tracks, requiring a one-to-one geometrical best matching ($\Delta R = \sqrt{\Delta\eta^2 + \Delta\phi^2}$) of a reconstructed online track with an offline one. For this kind of study, only reconstructed tracks passing a set of selection criteria are considered: at least 1 pixel hit and 6 SCT clusters, $|\eta| < 2.5$, $|z_0| < 200$ mm, $|d_0| < 1.5$ mm (both impact parameters z_0 and d_0 are calculated w.r.t. the reconstructed offline primary vertex).

The data used in the following for these performance studies are taken from LHC stable beam collisions with inner detector components and magnetic solenoid fully operational. In addition,

comparisons between data and non-diffractive minimum bias Monte Carlo (MC) simulated events are presented.

The RoI selection mode previously described is designed to work with higher energy physics objects, while data taken at $\sqrt{s} = 900$ GeV contain mostly soft events. At this stage, there was not enough statistics of collected tracks from an RoI-based trigger. Therefore, during 900 GeV collisions the HLT algorithms worked in *full scan* mode, retrieving data from the whole inner detector. This mode of operation is adopted for the beam spot determination and for online selection of B-physics decay channels.

Comparisons between the number of Si hits w.r.t. MC/offline and efficiency vs p_T for 900 GeV collisions data are shown in Fig. 1–4 for both L2 and EF algorithms.

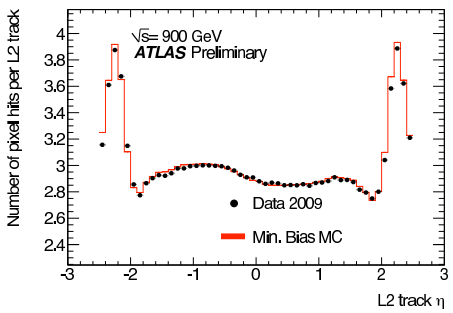

Figure 1: Average number of pixel hits per L2 track (data and MC).

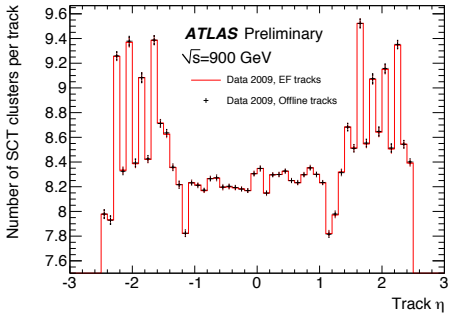

Figure 2: Average number of SCT hits per EF track (data and offline).

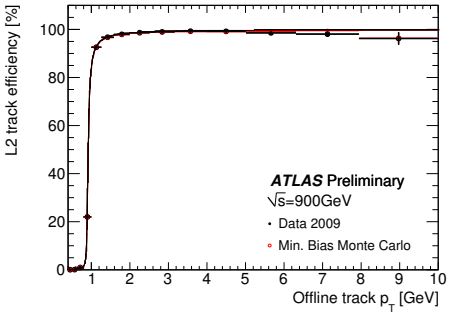

Figure 3: L2 tracking efficiency vs p_T w.r.t. offline (data and MC).

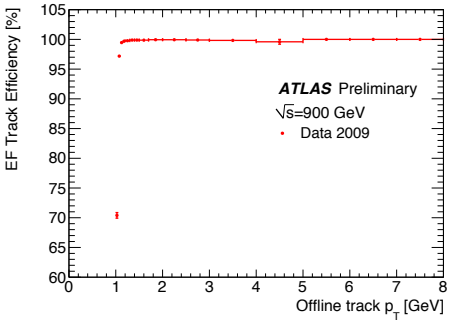

Figure 4: EF tracking efficiency vs p_T w.r.t. offline (data).

Figure 1 and Fig. 2 show an excellent agreement between data and MC/offline; complementary plots of L2 SCT hits and EF pixel hits are not presented, but show agreement at the same level. Figure 3 and Fig. 4 prove very good tracking efficiency w.r.t. offline. Figure 3 shows also excellent agreement between data and MC performance. More detailed results about 900 GeV tracking performance can be found in [2].

For the previously discussed reasons, collision data taken at $\sqrt{s} = 7$ TeV, with increased luminosity, represent the first opportunity to test the performance of RoI-based selections with real data.

In the following, the tracking efficiencies for muon and jet selections are presented. The track reconstruction for muons and jets starts from different RoIs ($\Delta\eta$, $\Delta\phi = 0.2$ and $\Delta\eta$,

$\Delta\phi = 0.4$, respectively). For muons, the reconstructed tracks are then matched to the muon spectrometer, while for jets a precise estimate of the track parameters at the perigee is crucial to identify tracks coming from secondary vertices for jet flavour tagging purposes.

Figures 5–6 show the muon and jet tracking efficiencies vs p_T during collision data taking at $\sqrt{s} = 7$ TeV. In both selections the HLT tracking algorithms show a very good reconstruction efficiency.

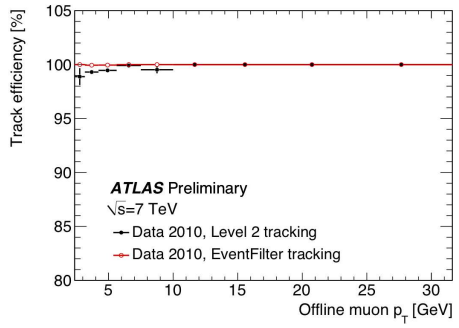

Figure 5: L2 and EF muon tracking efficiency vs p_T w.r.t. offline.

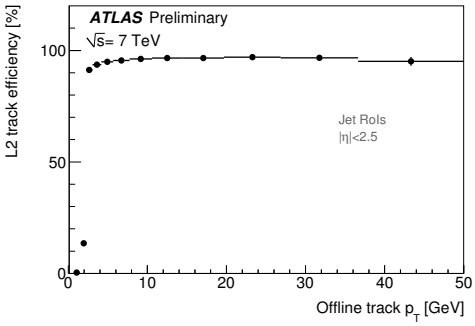

Figure 6: L2 jet tracking efficiency vs p_T w.r.t. offline.

As already mentioned, L2 tracking is used in the online determination of the beam spot, i.e. the transverse position of the LHC luminous region, crucial for all the selections which require a precise estimate of the interaction point (jet flavour tagging, monitoring of beam profile). L2 algorithms allow for an estimation of the beam spot mean position using the transverse distribution of online reconstructed primary vertices. Online primary vertices are obtained by fitting together all the L2 tracks reconstructed in full scan mode.

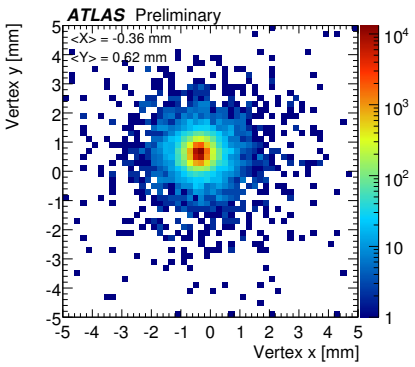

Figure 7: xy-distribution of the online L2 vertices.

Figure 7 shows the xy-distribution of online primary vertices during collision data taking at $\sqrt{s} = 7$ TeV: beam spot mean position and width are extracted by a gaussian fit of this distribution. Excellent agreement has been observed w.r.t. offline beam spot measurements.

ATLAS HLT algorithms have been successfully run online at the LHC since December 2009, at a centre-of-mass energy of 900 GeV and 7 TeV: it was shown that performance studies w.r.t offline tracks and MC simulations are in excellent agreement. Moreover, the performance of reconstructing tracks in the trigger system has been studied over time and changing beam conditions, producing very encouraging results. Furthermore, L2 tracks have been used to determine online the position of the LHC luminous region.

References

[1] ATLAS Collaboration, "The ATLAS Experiment at the CERN Large Hadron Collider," JINST 3 (2008) S08003.

[2] ATLAS Collaboration, "Performance of the ATLAS Inner Detector Trigger algorithms in p-p collisions at $\sqrt{s} = 900$ GeV," ATLAS-CONF-2010-014 (2010).

MSSM Higgs Boson Production via Gluon Fusion

Margarete Mühlleitner[1], *Heidi Rzehak*[1]*, *Michael Spira*[2]

[1]KIT, ITP, Wolfgang-Gaede-Str. 1, 76128 Karlsruhe, Germany
[2]Paul Scherrer Institut, 5232 Villigen PSI, Switzerland

DOI: http://dx.doi.org/10.3204/DESY-PROC-2010-01/rzehak

One major task at the LHC is the search for Higgs bosons. In the Minimal Supersymmetric Standard Model (MSSM), the cross section of the production process of Higgs bosons via gluon fusion, $gg \to h, H$, yields the largest values for a wide range of the MSSM parameters. This process is loop-induced where, in the MSSM, the coupling of the Higgs boson to the gluons is not only mediated by top and bottom quark loops as in the Standard Model (SM) but also by the corresponding squark loops (see Fig. 1). For large $\tan\beta$, which denotes the ratio of the two vacuum expectation values of the two complex Higgs doublets introduced in the MSSM, the coupling of bottom quarks to the Higgs bosons is enhanced. Therefore, for large $\tan\beta$, also bottom quark as well as bottom squark loops contribute sizeably to the gluon fusion cross section.

Pure QCD and Supersymmetric QCD Contributions

The pure QCD corrections to quark and squark loops (see Fig. 1 (b)) have been calculated at next-to-leading order taking into account the full mass dependence [1]. An increase of the cross section by up to 100% has been found. Theses corrections can be approximated by the limit of very heavy top quark and squarks with an accuracy of 20% – 30% for small $\tan\beta$ [2] (for large $\tan\beta$ also bottom quark and squark loops have to be taken into account). In the heavy top quark mass limit — without squark effects — the next-to-next-to-leading order (NNLO) QCD corrections have been calculated which resulted in an increase of 20% – 30% of the cross section [3]. At NNLO finite top quark mass effects (no squarks) have been discussed and found to be below the scale uncertainty [4]. Estimates of the next-to-next-to-next-to-leading order (N^3LO) corrections indicate an improved convergence [5].

The supersymmetric (SUSY) as well as the pure QCD contributions, taking into account gluino as well as gluon contributions (see Fig. 1 (c) as well as (b)), have been calculated in the heavy top quark, top squark and gluino limit [6]. The size of the next term in the mass expansion indicates that this is a good approximation for the lightest MSSM Higgs boson for small and moderate $\tan\beta$ values. Most recently, also the pure and the SUSY QCD contributions to the bottom quark and squark loops have been calculated based on an asymptotic expansion in the squark and gluino masses which are assumed to be much heavier than the bottom quark and the Higgs boson [7].

The pure and the SUSY QCD corrections have been calculated including the mass dependence of all particles and also the bottom quark and squark contributions [8]. This calculation

*Speaker

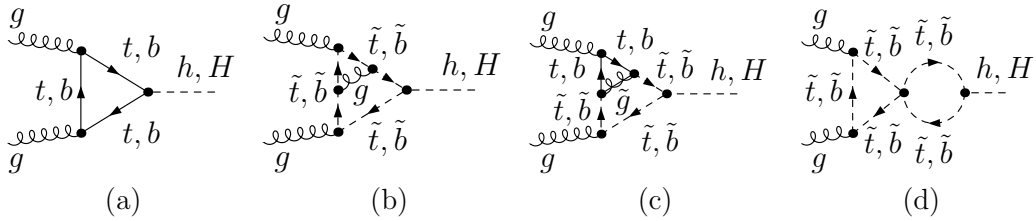

Figure 1: Sample diagrams which contribute to the gluon fusion process at (a) leading order and (b), (c), (d) next to leading order.

has shown that the heavy mass limit is a good approximation for small and moderate $\tan\beta$. Also, it was pointed out that the contributions from the squark quartic couplings (see Fig. 1 (d)) as well as from the gluinos can be sizeable.

This leads us to a conceptional problem: On the one hand if the supersymmetric relations between the parameters are kept intact the gluinos do not decouple. To be more precise, for heavy gluinos, the results of the form factors depend logarithmically on the gluino mass $M_{\tilde{g}}$. On the other hand the decoupling theorem says that heavy fields decouple at low momenta (except for renormalization effects) [9].

Decoupling of the Gluinos

Assuming vanishing squark mixing, for scales *above* the gluino mass, the coupling of the light CP-even Higgs boson to quarks λ_Q and the coupling of the same Higgs boson to squarks $\lambda_{\tilde{Q}}$ can be expressed as

$$\lambda_Q = g\,\frac{m_Q}{v} \quad \text{and} \quad \lambda_{\tilde{Q}} = 2\,g\,\frac{m_Q^2}{v} \tag{1}$$

where $v = (v_1^2 + v_2^2)^{\frac{1}{2}} \approx 246$ GeV and v_i is the i$^{\text{th}}$ Higgs vacuum expectation value. m_Q denotes the top quark mass and g is a normalization factor of the Higgs coupling to a quark pair with respect to the SM. Obviously, the symmetry relation between λ_Q and $\lambda_{\tilde{Q}}$ in Eq. 1 is intact. For the evaluation of λ_Q and $\lambda_{\tilde{Q}}$ at a different scale the corresponding renormalization group equations (RGE) can be used. In the assumed case of scales *above* the gluino mass, the RGE for $2\,\frac{v}{g}\,\lambda_Q^2$ and for $\lambda_{\tilde{Q}}$ are the same.

For scales *below* the gluino mass, the gluino decouples from the RGE and the RGE for $2\,\frac{v}{g}\,\lambda_Q^2$ and for $\lambda_{\tilde{Q}}$ differ. The symmetry relation between λ_Q and $\lambda_{\tilde{Q}}$ is broken.

At the scale of the gluino mass the proper matching yields a finite threshold contribution for the evolution from the gluino mass scale to smaller scales. The logarithmic behaviour of the matching relation is given by the solution of the RGE for smaller scales.

If the decoupling of the gluino is taken into account in the RGE the gluino also decouples from the theory as it should according to the decoupling theorem (for more details, see [10]).

Genuine SUSY QCD Contributions

In Fig. 2, first results of the calculation of the genuine SUSY QCD contributions to the bottom quark and squark amplitudes are shown in terms of the form factor C^b_{SUSY} normalized to

the bottom quark form factor A_b^{Higgs}:

$$A_b^{\text{Higgs}}(1 + C^b_{\text{SUSY}}\frac{\alpha_s}{\pi}) \,. \qquad (2)$$

The parameters are chosen as follows: The sfermion mass parameter $M_{\text{SUSY}} = 800$ GeV, the gluino mass $M_{\tilde{g}} = 1.0$ TeV, the gaugino mass parameter $M_2 = 500$ GeV, the Higgs superfield mixing parameter $\mu = 2.0$ TeV, $\tan\beta = 30$ and the trilinear coupling chosen in the $\overline{\text{MS}}$ scheme as $A_b = -1.133$ TeV. The SUSY QCD contributions with the full mass dependence (solid lines) are sizeable and can be roughly approximated using a correct bottom Yukawa coupling. This approximation is referred to as Δ_b approximation (dashed lines). It is important to choose the renormalization carefully. Using the trilinear coupling A_b in the $\overline{\text{MS}}$ scheme is one reasonable choice (for further details, see [11]).

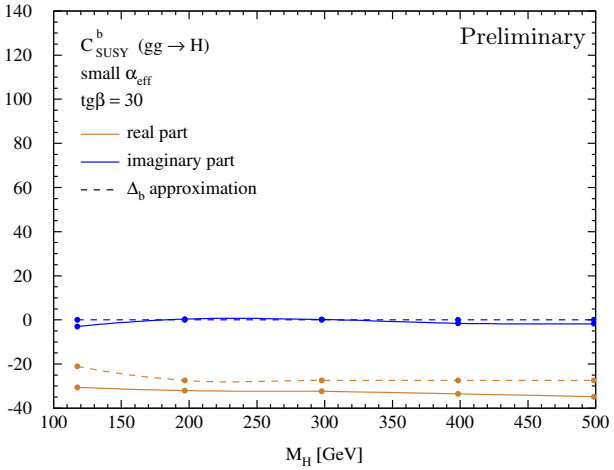

Figure 2: The genuine SUSY QCD contributions in terms of the form factor C^b_{SUSY} normalized to the bottom quark form factor: Real part in orange (light gray), imaginary part in blue (dark gray). The result with the full mass dependence (solid) is compared to the one in the Δ_b approximation (dashed).

References

[1] D. Graudenz, M. Spira, P.M. Zerwas, Phys. Rev. Lett. **70** (1993) 1372; M. Spira, A. Djouadi, D. Graudenz, P.M. Zerwas, Phys. Lett. **B318** (1993) 347; Nucl. Phys. **B453** (1995) 17; C. Anastasiou, S. Beerli, A. Daleo, Z. Kunszt, JHEP **0701** (2007) 082; U. Aglietti, R. Bonciani, G. Degrassi, A. Vicini, JHEP **0701** (2007) 021; R. Bonciani, G. Degrassi, A. Vicini, JHEP **0711** (2007) 095; M. Mühlleitner, M. Spira, Nucl. Phys. **B790** (2008) 1.

[2] A. Djouadi, M. Spira, P.M. Zerwas, Phys. Lett. **B264** (1991) 440; S. Dawson, Nucl. Phys. **B359** (1991) 283; R.P. Kauffman, W. Schaffer, Phys. Rev. **D49** (1994) 551; S. Dawson, R. Kauffman, Phys. Rev. **D49** (1994) 2298; S. Dawson, A. Djouadi, M. Spira, Phys. Rev. Lett. **77** (1996) 16; M. Krämer, E. Laenen, M. Spira, Nucl. Phys. **B511** (1998) 523.

[3] R.V. Harlander, W.B. Kilgore, Phys. Rev. Lett. **88** (2002) 201801; JHEP **0210** (2002) 017; C. Anastasiou, K. Melnikov, Nucl. Phys. **B646** (2002) 220; Phys. Rev. **D67** (2003) 037501; V. Ravindran, J. Smith, W.L. van Neerven, Nucl. Phys. **B665** (2003) 325.

[4] R.V. Harlander, K.J. Ozeren, Phys. Lett. **B679** (2009) 467; JHEP **0911** (2009) 088; A. Pak, M. Rogal, M. Steinhauser, Phys. Lett. **B679** (2009) 473; JHEP **1002** (2010) 025; R. V. Harlander, H. Mantler, S. Marzani, K. J. Ozeren, Eur. Phys. J. C **66** (2010) 359.

[5] S. Catani, D. de Florian, M. Grazzini, P. Nason, JHEP **0307** (2003) 028; S. Moch, A. Vogt, Phys. Lett. **B631** (2005) 48; V. Ravindran, Nucl. Phys. **B746** (2006) 58; Nucl. Phys. **B752** (2006) 173.

[6] R.V. Harlander, M. Steinhauser, Phys. Lett. **B574** (2003) 258, Phys. Rev. **D68** (2003) 111701; JHEP **0409** (2004) 066; R.V. Harlander, F. Hofmann, JHEP **0603** (2006) 050; G. Degrassi, P. Slavich, Nucl. Phys. **B805** (2008) 267.

[7] G. Degrassi, P. Slavich, arXiv:1007.3465 [hep-ph].

[8] C. Anastasiou, S. Beerli, A. Daleo, Phys. Rev. Lett. **100** (2008) 241806.

[9] T. Appelquist, J. Carazzone, Phys. Rev. **D11** (1975) 2856.

[10] M. Mühlleitner, H. Rzehak, M. Spira, JHEP **0904** (2009) 023.

[11] M. Mühlleitner, H. Rzehak, M. Spira, PoS **RADCOR2009** (2010) 043, arXiv:1001.3214 [hep-ph].

Inclusive and associated b-quark production in the Regge limit of QCD

Bernd A. Kniehl[1], *Vladimir Saleev*[2], *Alexandera Shipilova*[2*]

[1]Institut für Theoretische Physik, Universität Hamburg, Luruper Chaussee 149, 22761 Hamburg, Germany
[2]Samara State University, Ak. Pavlova Street 1, 443011 Samara, Russia

DOI: http://dx.doi.org/10.3204/DESY-PROC-2010-01/shipilova

The study of b-jet production at high-energy colliders is of great interest for the test of perturbative quantum chromodynamics (QCD). The presence of a heavy b quark, with mass $m_b \gg \Lambda_{\rm QCD}$, where $\Lambda_{\rm QCD}$ is the asymptotic scale parameter of QCD, in such processes guarantees a large momentum transfer that keeps the strong-coupling constant small $\alpha_s(m_b) \lesssim 0.1$.

The total center-of-mass energy at the Tevatron, $\sqrt{S} = 1.96$ TeV in Run II, sufficiently exceeds the scale μ of the relevant hard processes, so that $\sqrt{S} \gg \mu \gg \Lambda_{\rm QCD}$. In this regime, the contributions to the production cross section from subprocesses involving t-channel exchanges of partons (gluons and quarks) may become dominant. Then, the off-shell properties of the incoming partons can no longer be neglected, and t-channel partons become Reggeized. In this so-called quasi-multi-Regge kinematics (QMRK), the particles (multi-Regge) or groups of particles (quasi-multi-Regge) produced in the collision are strongly separated in rapidity. For the inclusive b-jet production, this implies that a single b quark is produced in the central region of rapidity, while other particles, including a $\bar{b}$ quark, are produced at large rapidities. In the case of $b\bar{b}$ pair and $b\gamma$ associated production in the central rapidity region, we also assume that there are no other particles in this region, so that these particles are considered as quasi-multi-Regge pairs. The QMRK approach [1] is particularly appropriate for this kind of high-energy phenomenology. It is based on an effective quantum field theory implemented with the non-Abelian gauge-invariant action including fields of Reggeized gluons [2] and quarks [3].

First, we investigate inclusive single b-jet production in $p\bar{p}$ collisions. To leading order (LO) in the QMRK approach, there is only one partonic subprocess, $Q_b + R \to b(k)$ [4], where R and Q_b are the Reggeized gluon and b quark (with four-momentum k), respectively. At next-to-leading order (NLO), the main contribution arises from the partonic subprocess $R + R \to b + \bar{b}$, where the b and $\bar{b}$ quarks are produced close in rapidity, and its squared amplitude was obtained in Ref. [5]. In Fig. 1(a), the preliminary data presented by the CDF Collaboration [6] are compared with our predictions. Throughout all our analysis, the renormalization and factorization scales are chosen to be $\mu = \xi k_T$, where $1/2 \le \xi \le 2$, and the resulting theoretical uncertainties are indicated as shaded bands. In Fig. 1(a), we observe that the contribution due to LO subprocess greatly exceeds the one due to NLO subprocess and practically exhausts the full result. It nicely agrees with the CDF data throughout the entire k_T range.

*Speaker

In our analysis, we adopt the Kimber-Martin-Ryskin prescription [7] for unintegrated parton distribution functions (PDFs), using as input the Martin-Roberts-Stirling-Thorne collinear PDFs of the proton [8].

$b\bar{b}$-dijet production receives contributions from both subprocess $R + R \to b + \bar{b}$ and the annihilation of a Reggeized quark-antiquark pair, $Q_q + \bar{Q}_q \to b + \bar{b}$, where $q = u, d, s, c, b$. The induced vertex of the latter was obtained in Ref. [3] and the squared amplitudes in Ref. [9]. The CDF data [10] as distributions in the leading-jet (jet with the maximal transverse energy) transverse energy E_{1T}, the dijet invariant mass $M_{b\bar{b}}$, and the azimuthal separation angle $\Delta\phi$ are compared with our QMRK predictions in Figs. 1(b)–(d), where the two LO contributions are shown separately along with their superpositions. We observe that the total QMRK predictions nicely describe all the three measured cross section distributions. The contributions due to Reggeized gluon fusion dominate for $E_{1T} \lesssim 200$ GeV and $M_{b\bar{b}} \lesssim 300$ GeV and over the whole $\Delta\phi$ range considered. The peak near $\Delta\phi = 0.4$ in Fig. 1(d) arises from the isolation cone condition $R_{\rm cone} = \sqrt{\Delta y^2 + \Delta\phi^2} > 0.4$.

At last, there are two mechanisms of photon-associated b-quark production: direct photon production via the LO partonic subprocess in the QMRK $Q_b + R \to b + \gamma$ [11], and the fragmentation of final-state partons into photons. In Figs. 1(e)–(f), we observe that the contribution due to direct photon production greatly exceeds the one due to photon production by fragmentation, by about of one order of magnitude at $k_{T\gamma} > 40$ GeV and by about a factor 5 at $k_{T\gamma} \approx 30$ GeV. The direct photon contribution practically exhausts the full result. It nicely agrees with the D0 data [12] throughout the entire $k_{T\gamma}$ range considered.

The work of B.A.K. was supported in part by BMBF Grant No. 05H09GUE, by DFG Grant No. KN 365/7–1, and by HGF Grant No. HA 101. The work of V.A.S. and A.V.S. was supported in part by the Federal Agency for Education of the Russian Federation under Contract No. P1338. The work of A.V.S. was also supported in part by the International Center of Fundamental Physics in Moscow and the Dynastiya Foundation.

References

[1] V. S. Fadin, L. N. Lipatov, Nucl. Phys. B **406** (1993) 259; Nucl. Phys. B **477** (1996) 767 [arXiv:hep-ph/9602287].

[2] L. N. Lipatov, Nucl. Phys. B **452** (1995) 369 [arXiv:hep-ph/9502308].

[3] L. N. Lipatov, M. I. Vyazovsky, Nucl. Phys. B **597** (2001) 399 [arXiv:hep-ph/0009340].

[4] V. A. Saleev, Phys. Rev. D **78** (2008) 034033 [arXiv:0807.1587v1[hep-ph]]; Phys. Rev. D **78** (2008) 114031 [arXiv:0812.0946v1[hep-ph]].

[5] V. A. Saleev, D. V. Vasin, Phys. Lett. B **605** (2005) 311 [arXiv:hep-ph/0411109].

[6] T. Aaltonen [CDF Collaboration], CDF note 8418 (2006), URL: `http://www-cdf.fnal.gov/physics/new/qcd/QCD.html`.

[7] M. A. Kimber, A. D. Martin, M. G. Ryskin, Phys. Rev. D **63** (2001) 114027 [arXiv:hep-ph/0101348].

[8] A. D. Martin, R. G. Roberts, W. J. Stirling, R. S. Thorne, Phys. Lett. B **531** (2002) 216 [arXiv:hep-ph/0201127].

[9] B. A. Kniehl, V. A. Saleev, A. V. Shipilova, Phys. Rev. D **81** (2010) 094010 [arXiv:1003.0346v2[hep-ph]].

[10] T. Aaltonen [CDF Collaboration], CDF note 8939 (2007), URL: `http://www-cdf.fnal.gov/physics/new/qcd/QCD.html`.

[11] V. A. Saleev, in Proc. of the XVII International Workshop on DIS and Related Topics, Madrid, Spain, 2009, `http://dx.doi.org/10.3360/dis.2009.103`.

[12] V. Abazov [D0 Collaboration], Phys. Rev. Lett. **102** (2009) 192002 [arXiv:0901.0739v2[hep-ex]].

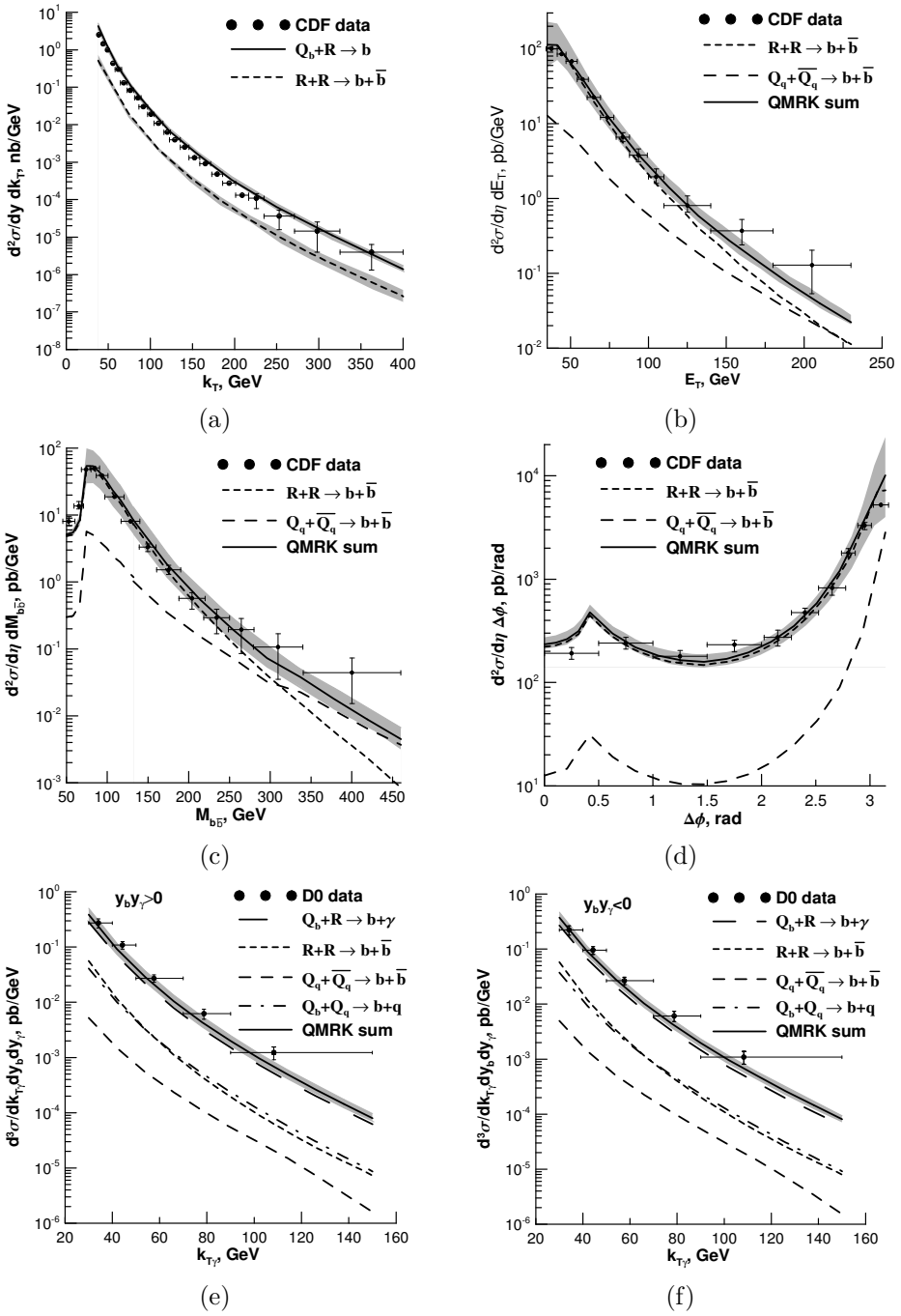

Figure 1: The distribution in (a) transverse momentum of inclusive single b-jet hadroproduction [6], the ones in (b) leading-jet transverse energy, (c) dijet invariant mass, and (d) azimuthal separation angle of inclusive $b\bar{b}$-dijet hadroproduction [10], and the ones in transverse momentum of $b\gamma$ hadroproduction [12] for (e) $y_b y_\gamma > 0$ and (f) $y_b y_\gamma < 0$ are compared with the QMRK predictions.

Physics potential of the CMS CASTOR forward calorimeter

Dmytro Volyanskyy for the CMS Collaboration
DESY, Notketraße 85, 22607 Hamburg, Germany

DOI: http://dx.doi.org/10.3204/DESY-PROC-2010-01/volyanskyy

The CASTOR calorimeter is a detector covering the very forward region of the CMS experiment at the LHC. It surrounds the beam pipe with 14 longitudinal modules each of which consisting of 16 azimuthal sectors and allows to reconstruct shower profiles, separate electrons and photons from hadrons and search for phenomena with anomalous hadronic energy depositions. The physics program that can be performed with this detector includes a large variety of different QCD topics. In particular, the calorimeter is supposed to contribute to studies of low-x parton dynamics, diffractive scattering, multi-parton interactions and cosmic ray related physics in proton-proton and heavy-ion collisions. The physics capabilities of this detector are briefly summarized in this paper.

1 Detector overview

The CASTOR (Centauro And STrange Object Reseacrh) detector is located at a distance of 14.4 m from the CMS interaction point right behind the Hadronic Forward (HF) calorimeter and the T2, a tracking station of the TOTEM experiment, covering the pseudorapidity region $-6.6 < \eta < -5.2$. This is a quartz-tungsten Cerenkov sampling calorimeter. That is, it is made of repeating layers (arranged in a sandwich structure) of quartz and tungsten plates. The former is used as the active material because of its radiation hardness, while the latter serves as the absorber medium providing the smallest possible shower size. The signal in CASTOR is produced when charged shower particles pass through the quartz plates with the energy above the Cerenkov threshold (190 keV for electrons). The generated Cerenkov light is then collected by air-code light guides, which are transmitting it further to photo-multipliers tubes PMTs. These devices produce signals proportional to the amount of light collected. As can be seen in Figure 1, the detector plates are tilted at 45° w.r.t. the beam axis to maximaize the Cerenkov light output in the quartz. The CASTOR detector is a compact calorimeter with the physical size of

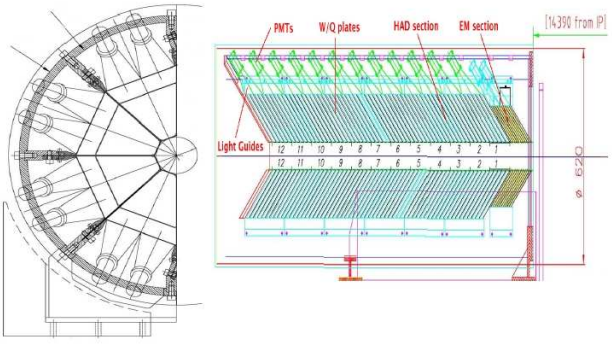

Figure 1: *Sketch of the CASTOR calorimeter: front view (left) and longitudinal cross section (right).*

about 65 cm × 36 cm × 150 cm and having no segmentation in η. It is embedded into a skeleton, which is made of stainless steel. The detector consists of 14 longitudinal modules, each of which comprises 16 azimuthal sectors that are mechanically organized in two half calorimeters. First 2 longitudinal modules form the electromagnetic section, while the other 12 modules form the hadronic section. In the electromagnetic section, the thicknesses of the tungsten and quartz plates are 5.0 and 2.0 mm, respectively. The corresponding thicknesses in the hadronic section are twice as large as in the electromagnetic section. With this design, the diameter of the showers of electrons and positrons produced by hadrons is about one cm, which is an order of magnitude smaller than in other types of calorimeters. The detector has a total depth of 10.3 interaction lengths and includes 224 readout channels. It should be noted that the final CASTOR design is the result of three test beam campaigns and numerous Monte Carlo simulations. After the completion of the detector construction in the spring of 2009, the calorimeter has been successfully installed and commissioned in the summer of 2009.

2 The CASTOR physics capabilities

Because of its pseudorapidity coverage, CASTOR significantly expands the CMS capability to investigate physics processes occurring at very low polar angles and so, providing a valuable tool to study low-x QCD, diffractive scattering, multi-parton interactions and underlying event structure. Another CASTOR objective is to search for exotic objects with unusual longitudinal shower profile, several of which have been observed in cosmic ray experiments.

2.1 Low-x QCD

A study of QCD processes at a very low parton momentum fraction $x = p_{\text{parton}}/p_{\text{hadron}}$ is a key to understand the structure of the proton, whose gluon density is poorly known at very low values of x. At the LHC the minimum accessible x in proton-proton (pp) collisions decreases by a factor of about 10 for each 2 units of rapidity. This implies that a process with a hard scale of $Q \sim 10$ GeV and within the CASTOR acceptance can probe quark densities down $x \sim 10^{-6}$ [1], that has never been achieved before. Such processes include the production of forward jets and Drell-Yan electron pairs. The latter occurs via the $qq \rightarrow \gamma^* \rightarrow e^+e^-$ reaction within the acceptance of CASTOR and TOTEM-T2 station, whose usage is essential for detecting these events. Measurements of Drell-Yan events can also be used to study QCD saturation effects – the effects of rising of the gluon density in the proton with decreasing values of x, that have been firstly observed at HERA. It was found that the Drell-Yan production cross section is suppressed roughly by a factor of 2 when using a PDF with saturation effects compared to one without. Another way to constrain the parton distribution function (PDF) of the proton at low x is provided by measuring forward jets in CASTOR that will enable to probe the parton densities down 10^{-6}. Moreover, this allows to gain information on the full QCD evolution to study high order QCD reactions. Apart from that, it has been found that a BFKL like simulation, for which the gluon ladder is ordered in x, predicts more hard jets in the CASTOR acceptance than the DGLAP model that assumes strong ordering in the transverse momentum k_{T} and random walk in x. Therefore, measurements of forward jets in CASTOR can be used as a good tool to distinguish between DGLAP and non-DGLAP type of QCD evolution. Furthermore, CASTOR in combination with HF can be used to measure Mueller-Navalet dijet events, which are characterized by two jets with similar p_{T} but large rapidity separation. By measuring Mueller-Navalet dijets in CASTOR one can probe BFKL-like dynamics and small-x evolution.

2.2 Diffraction

A good way to study the perturbative QCD and the hadron structure is provided by diffractive pp interactions (where one or both the colliding protons stay intact) via measurements of the cross sections for diffractive W, Z, jet or heavy quark productions. The CASTOR calorimeter is, in particular, a very useful tool to measure the single-diffractive productions of W and dijets in pp collisions ($pp \to pX$ reaction, where X is either a W boson or a dijet system). These are hard diffractive processes that are sensitive to the quark and gluon content of the low-x proton PDFs, correspondingly. A selection of such events can be performed using the multiplicity distributions of tracks in the central tracker and calorimeter towers in HF plus CASTOR exploiting the fact that diffractive events on average have lower multiplicity in the central region and in the "gap side" than non-difractive ones. Feasibility studies to detect the single-diffractive productions of W [2] and dijets [3] have shown that the diffractive events peak in the regions of no activity in HF and CASTOR.

2.3 Multi-parton interactions and underlying event structure

Measurements of energy deposits in the CASTOR acceptance should significantly improve our understanding of the multi-parton interactions (MPI) and underlying event (UE) structure. The latter is an unavoidable background to most collider observables, whose understanding is essential for precise measurements at the LHC. It consists of particles arising from the beam-beam remnants and from MPI. The MPI arise in the region of small-x where parton densities are large so that the likelihood of more than one parton interaction per event is high. According to all QCD models, the larger the collision energy the greater the contribution from MPI to the hard scattering process. However, this dependence is currently weakly known. Measurements of the forward energy flow by means of CASTOR will allow to discriminate between different MPI models, which vary quite a lot. Furthermore, measurements of forward particle production in pp and Pb-Pb collisions at LHC energies with CASTOR should help to significantly improve the existing constraints on ultra-high energy cosmic ray models.

3 Conclusion

The CASTOR calorimeter is a valuable CMS subcomponent allowing to perform a very rich physics program. The detector is fully integrated in the CMS readout and currently take collision data. Its first physics results are currently under preparation.

4 Acknowledgments

I am very thankful to Hannes Jung, Kerstin Borras and many other colleagues working in the CMS forward physics community for fruitful discussions, suggestions and encouragements.

References

[1] *CMS and TOTEM Collaborations.* CERN/LHCC 2006-039/G-124 (2006).

[2] *CMS Collaboration.* CERN CMS-PAS-DIF-07-002 (2007).

[3] *CMS Collaboration.* CERN CMS-PAS-FWD-08-002 (2008).

The sensitivity of the ATLAS detector to the Standard Model Higgs boson in the four lepton final state

Craig Wiglesworth for the ATLAS Collaboration

Department of Physics, University of Liverpool, United Kingdom

DOI: http://dx.doi.org/10.3204/DESY-PROC-2010-01/wiglesworth

The Higgs boson is the only particle in the Standard Model (SM) that has not yet been discovered. Although its mass (m_H) is a free parameter, direct searches at the Large Electron Positron collider have set a lower limit on m_H of 114.4 GeV at 95% confidence level (CL) [1]. In addition, ongoing searches at the Tevatron have excluded the range $162 < m_H < 166$ GeV at 95% CL [2]. Assuming the overall validity of the SM, a global fit to precision electroweak data provides an indirect upper limit on m_H of 157 GeV at 95% CL [3].

The analyses described here were performed using detailed simulations of the ATLAS detector response to proton-proton collisions at a centre-of-mass energy of 14 TeV. Further details of the analyses can be found in [4].

The $H \to ZZ^{(*)} \to 4l$ channel is an important channel in the search for the SM Higgs boson as it provides one of the cleanest experimental signatures. In the range of m_H values considered, the dominant background to this channel is the $pp \to ZZ^{(*)} \to 4l$ continuum. Below about 200 GeV, where one of the Z bosons in the signal channel is produced off-shell, the $pp \to Zb\bar{b}$ and $pp \to t\bar{t}$ processes also contribute.

The online selection of candidate $H \to ZZ^{(*)} \to 4l$ events is performed either by single lepton or double lepton triggers. The offline event selection requires that the candidate events have at least four leptons that can be coupled into pairs of same flavour and opposite charge. The $4l$ invariant mass resolution is improved by 10% to 17% when applying a Z boson mass constraint to one (or both if $m_H > 200$) of the lepton pairs. The resulting 4μ invariant mass distribution in simulated signal events for $m_H = 130$ GeV is shown in Figure 1. A similar distribution is also observed for the $4e$ invariant mass.

The calorimeter isolation, track isolation and transverse impact parameter significance of the leptons in the candidate events are discriminating variables in the rejection of the $pp \to Zb\bar{b}$ and $pp \to t\bar{t}$ background processes. The track (calorimeter) isolation variable is defined as the total transverse momentum (total energy) deposit around the lepton, normalised to the transverse momentum of the lepton. The impact parameter significance is the transverse impact parameter of the lepton with respect to the primary vertex, divided by the corresponding measurement error. The $4l$ invariant mass distributions in simulated signal and background events after all event selection criteria are shown in Figure 2.

The signal significance is determined using two different approaches. In the first approach, the number of signal and background events are counted within a mass window of $m_H \pm 2\sigma$,

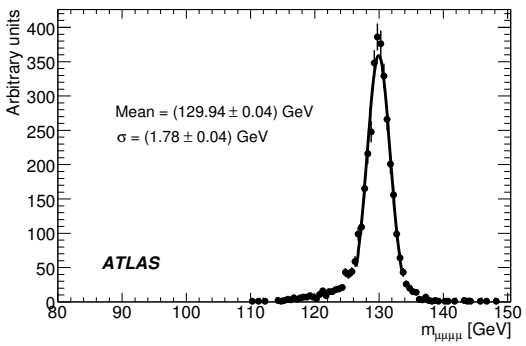

Figure 1: The 4μ invariant mass distribution in simulated signal events for $m_H = 130$ GeV.

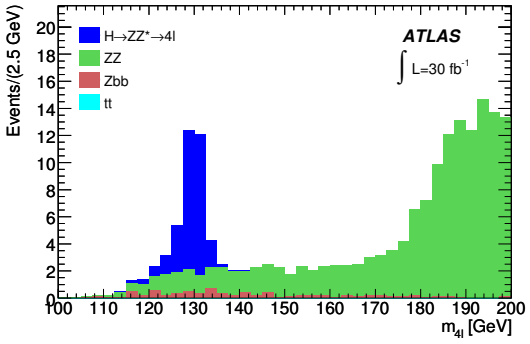

Figure 2: The $4l$ invariant mass distributions in simulated signal and background events after all event selection criteria for $m_H = 130$ GeV.

where σ is the experimental $4l$ invariant mass resolution. The significance is then calculated using Poissonian statistics without consideration of systematic uncertainties. In the second approach, the signal and background contributions are extracted from a fit to the $4l$ invariant mass distribution. The signal significance and exclusion limits are then calculated using a profile likelihood ratio method in which systematic uncertainties are taken into account. The 3% to 5% uncertainty on the signal selection efficiency is dominated by the experimental uncertainties relating to lepton reconstruction performance. The expected signal significance for an integrated luminosity of 30 fb^{-1} and the luminosity required for an exclusion at 95% CL in the $H \to ZZ^{(*)} \to 4l$ channel are shown in Figure 3 and Figure 4, respectively.

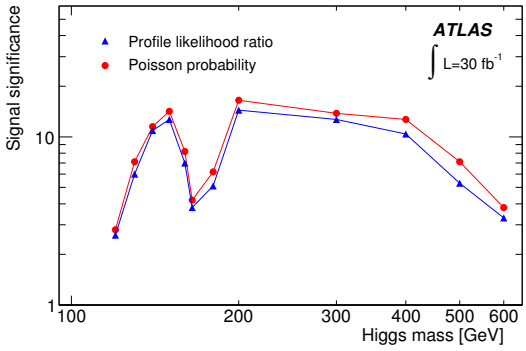

Figure 3: The expected signal significance for an integrated luminosity of 30 fb^{-1}.

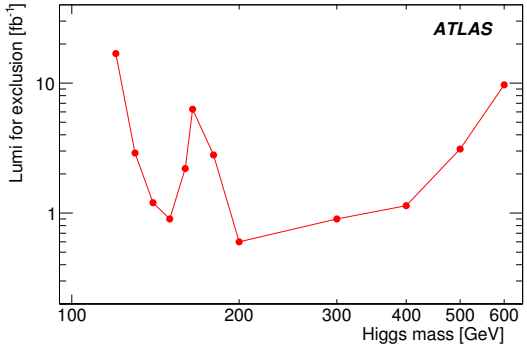

Figure 4: The luminosity required for an exclusion at 95% CL.

The $H \to ZZ^{(*)} \to 4l$ channel is combined with other important decay channels ($H \to W^+W^-$, $H \to \gamma\gamma$ and $H \to \tau^+\tau^-$) to provide a single measure of the significance of a discovery or an exclusion limit for various m_H values [4]. The expected combined discovery significances for an integrated luminosity of 10 fb^{-1} and the combined exclusion limits for an integrated luminosity of 2 fb^{-1} are shown in Figure 5 and Figure 6, respectively.

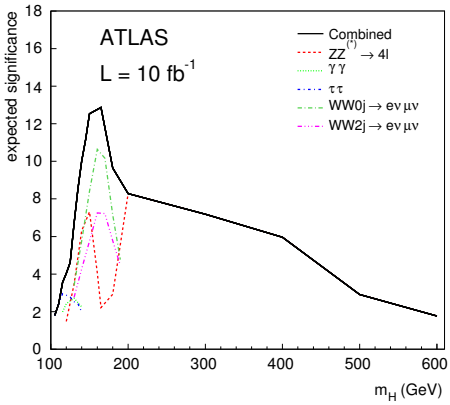

Figure 5: The expected combined discovery significances for an integrated luminosity of 10 fb^{-1}.

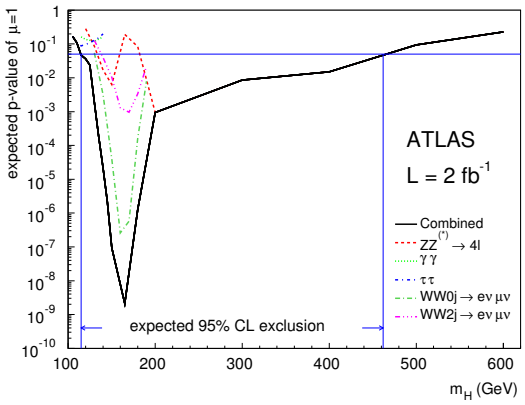

Figure 6: The expected combined exclusion limits for an integrated luminosity of 2 fb^{-1}.

With an integrated luminosity of 30 fb^{-1}, the expected sensitivity of the ATLAS detector to the discovery of the SM Higgs boson in the $H \to ZZ^{(*)} \to 4l$ channel alone is at the 5σ level or greater in the mass range $130 < m_H < 500$ GeV, with the exception of the region around 160 GeV where the branching ratio for $H \to ZZ^*$ decays is suppressed due to the opening of the phase space for the decay into two on-shell W bosons. With an integrated luminosity of 10 fb^{-1}, the expected combined sensitivity of the ATLAS detector to the discovery of the SM Higgs boson in the combination of channels is at the 5σ level or greater in the mass range $130 < m_H < 430$ GeV. For $m_H > 200$ GeV, the $H \to ZZ^{(*)} \to 4l$ channel will play a key role in the discovery or exclusion of the SM Higgs boson.

References

[1] R. Barate *et al.* [LEP Working Group for Higgs boson searches and ALEPH Collaboration], Phys. Lett. B **565** (2003) 61 [arXiv:hep-ex/0306033].

[2] T. Aaltonen *et al.* [CDF and D0 Collaborations], Phys. Rev. Lett. **104** (2010) 061802 [arXiv:1001.4162 [hep-ex]].

[3] J. Alcaraz [ALEPH Collaboration and CDF Collaboration and D0 Collaboration], arXiv:0911.2604 [hep-ex].

[4] G. Aad *et al.* [The ATLAS Collaboration], CERN-OPEN-2008-020.

Tile calorimeter at work in the collision era

Tibor Zenis on behalf of the ATLAS Tile Calorimeter Group

Comenius University in Bratislava, Safarikovo namestie 6, 818 06 Bratislava 16, Slovakia

DOI: http://dx.doi.org/10.3204/DESY-PROC-2010-01/zenis

1 Detector description

The Tile Calorimeter [1] is the central region hadronic calorimeter (Fig. 1 left) of the ATLAS experiment [2] at the CERN Large Hadron Collider.

The Tile Calorimeter is a sampling calorimeter using steel as absorber and scintillator plates as active medium. It is divided into a 5.8 m long central barrel and two 2.6 m long extended barrel cylinders, each having an inner radius 2.28 m and an outer radius of 4.25 m.

Each of the cylinders is composed of 64 azimuthal modules subtending $\Delta\phi = 0.1$. The Tile scintillator plates are placed perpendicular to the colliding beam axis, and are radially staggered in depth. The structure is periodic along the beam axis. Two sides of the scintillating tiles are read out by wave-length shifting (WLS) fibers into two separate photomultipliers (PMTs).

By the grouping of WLS fibers to specific PMTs, modules are segmented in pseudorapidity η and in radial depth. The resulting typical cell dimensions are $\Delta\eta \times \Delta\phi = 0.1 \times 0.1$.

This segmentation defines a quasi-projective tower structure. Altogether, Tile Calorimeter comprises 4672 read-out cells, each equipped with two PMTs that receive light from opposite sides of the tiles.

The Tile Calorimeter together with the central liquid argon electromagnetic calorimeter will measure the energy of particle jets and contribute to the determination of the missing transverse energy of events in the pseudorapidity range $|\eta| < 1.7$.

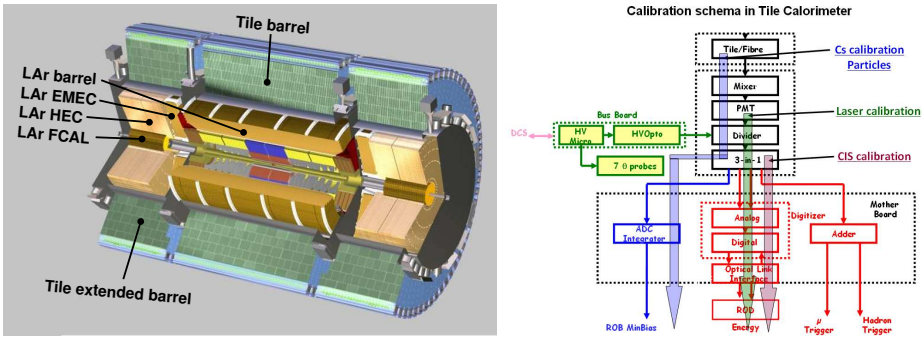

Figure 1: Left: View of the central part of ATLAS detector showing the tile calorimeter (tile barrel in center, tile extended barrels in side regions) surrounding the different segments of the liquid argon (LAr) calorimeter. Right: Calibration scheme in the tile calorimeter: Cs radioactive source, laser pulses, charge injection system.

2 Calibration

The Tile Calorimeter is equipped with a system that allows to monitor and to calibrate each stage of the read-out system exploiting different signal sources (Fig. 1 right).

The Charge Injection System sends charge pulses to each electronic channel. The system is designed to calibrate the read-out electronic system across all PMTs of the calorimeter at accuracy of 1 %. The Laser system provides light to all PMTs. It is designed to calibrate and monitor the response of the PMTs with a precision better than 0.5 %. The radioactive Cesium source ^{137}Cs moves through all Tile Calorimeter cells by a hydraulic system. The Cesium calibration system allows to obtain a uniformity of the cell response at the level of 0.3 %. [3]

3 Cosmic muons and splash events

The Tile Calorimeter response to cosmic and test-beam muons was used to measure the performance of the detector. The electromagnetic scale of the Tile Calorimeter modules was validated with the precision of 3 % using muons. Good agreement between data and Monte Carlo (MC) in test-beam and cavern muon data was observed.

The time offsets of the Tile Calorimeter cells were measured with cosmic muons and single beam data. The results agree within a precision of 1 ns.

In the splash events the LHC beam hits a completely closed collimator 140 m far from the center of the ATLAS and secondary particles penetrate all ATLAS detectors. The Tile Calorimeter cells timing after time-of-flight correction was validated (Fig. 2 left) and RMS = 0.45 ns was achieved for cells with proper time calibration.

4 Collisions

The distribution of the Tile Calorimeter cell response was compared with collision data at 7 TeV, 2.36 TeV, 900 GeV, minimum bias MC and randomly triggered events (Fig. 2 right). Good agreement between data and MC was observed.

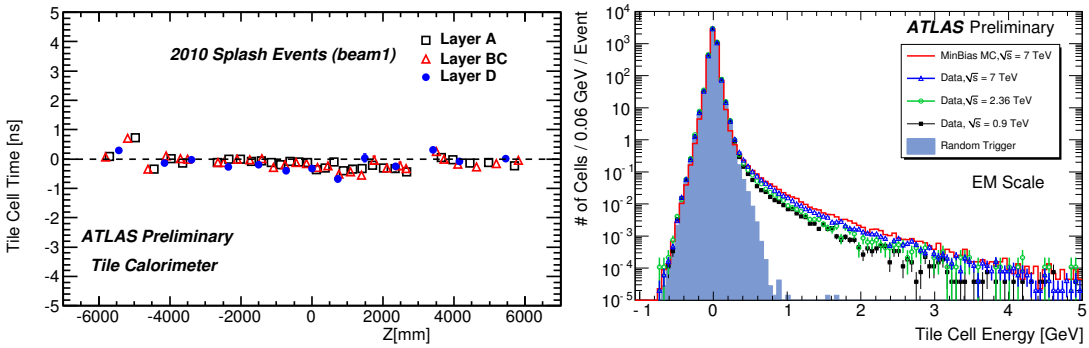

Figure 2: Left: The average cell time as a function of the cell Z (along beam axis) coordinate. Timing corrections based on the time of flight had been applied. Right: Energy of the tile calorimeter cells. The distributions from collision data at 7 TeV, 2.36 TeV, and 0.9 TeV are superimposed with Pythia minimum bias Monte Carlo and randomly triggered events.

The Tile Calorimeter cell response uniformity as a function of pseudorapidity η and azimuthal angle ϕ was compared between collision events at 7 TeV and non-diffractive minimum bias MC events (Fig. 3). A nice match between MC and data was seen.

The online signal reconstruction by the ROD/DSP Optimal Filtering Non Iterative reconstruction [4] was validated with the collision events as well as out of time events. It was shown that linearity of online algorithm is within a few percent in the significant time range $[-10, 10]$ ns.

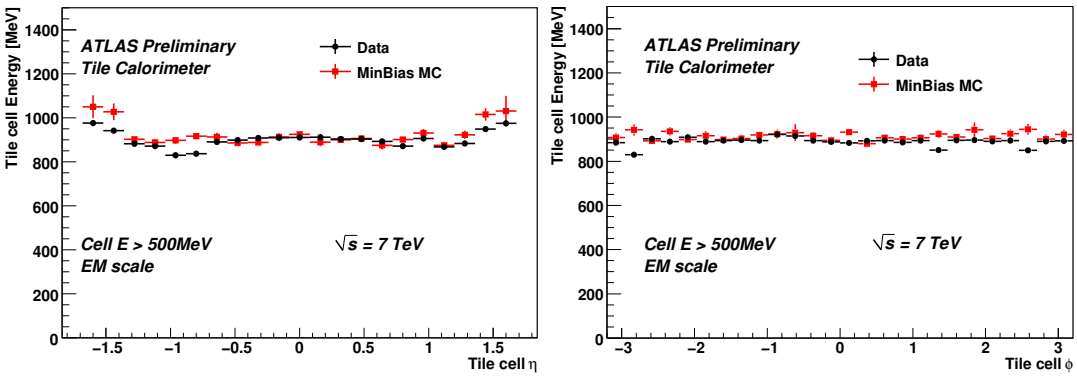

Figure 3: Tile calorimeter cell response uniformity as a function of pseudorapidity (left) and azimuthal angle (right) for 7 TeV collision and MC events.

5 Conclusion

The performance of the Tile Calorimeter has been measured and monitored using calibration data, random triggered data, cosmic muons, splash events and collision events.

The results of these studies give important information that assess the uniformity, the stability and the resolution of the energy measurements and, in general, the quality of the data description as given by the simulation of the Tile Calorimeter detector.

The performance and the quality of understanding the Tile Calorimeter is demonstrated. The detector is ready to detect hadrons, jets and to measure the missing transverse energy.

Acknowledgements

I acknowledge the support from the Ministry of Education of the Slovak Republic.

References

[1] [ATLAS Collaboration], "ATLAS tile calorimeter: Technical design report," CERN-LHCC-96-42.

[2] G. Aad *et al.* [ATLAS Collaboration], "The ATLAS Experiment at the CERN Large Hadron Collider," JINST **3** (2008) S08003.

[3] [The ATLAS Collaboration], "Readiness of the ATLAS Tile Calorimeter for LHC collisions," to be submitted to EPJC, (2010)

[4] A. Valero, "The ATLAS TileCal Read-Out Drivers Signal Reconstruction," ATL-TILECAL-PROC-2009-004, http://cdsweb.cern.ch/record/1223960

Recent performance results with the ATLAS Muon Spectrometer

Giovanni Zevi Della Porta for the ATLAS Muon Collaboration

Harvard University, Cambridge, MA 02138, United States of America

DOI: http://dx.doi.org/10.3204/DESY-PROC-2010-01/zevidellaporta

The ATLAS Muon Spectrometer (MS) is used to trigger on muons and reconstruct their tracks. It is composed of two sets of air-core superconducting toroidal magnets embedded in three layers of precision chambers and three layers of trigger chambers. Monitored Drift Tubes (MDT) and Cathode Strip Chambers (CSC) measure the bending coordinate (η) with a point resolution of respectively 80 and 60 μm. Resistive Plate Chambers (RPC) in the Barrel ($|\eta| < 1$) and Thin Gap Chambers (TGC) in the Endcap ($1 < |\eta| < 2.7$) also provide the second coordinate (ϕ) and the trigger signal (up to $|\eta| < 2.4$), with a point resolution around 1 cm.

Different types of muon tracks can be reconstructed using different combinations of subdetectors. Stand-alone tracks are based only on MS hits. The MS hits are used to form local straight segments, which are combined to form a curved track. The track parameters are then extrapolated, accounting for energy loss in the calorimeters, to the Interaction Point. Combined tracks are formed by matching a stand-alone track with an Inner Detector (ID) track, improving the precisionon of the track parameters, especially at low momenta. Tagged tracks are built from extrapolated ID tracks by looking for either a segment in the MS or energy depositions compatible with an isolated muon in the calorimeters. They are designed to increase tracking efficiency for low momentum muons or muons traversing uninstrumented areas (cracks).

The first set of performance studies on which we report is based on a large sample of RPC-triggered cosmic-ray events crossing the MS Barrel, recorded in the fall of 2009. Of these events, 48 million were collected without a toroidal B-field. For 21 million events the B-field was at nominal value (with a field integral between 2 and 8 Tm) in order to study momentum resolution and tracking efficiency.

Chamber alignment and sagitta resolution are studied using cosmic-ray tracks collected without magnetic field. The segment sagitta is defined as the distance from the Middle-station segment to the straight line connecting the segments in the Inner and Outer stations. The segment sagitta distribution for each sector is fitted to a double Gaussian (see Fig. 1(a)). The mean of the narrow Gaussian is used for track-based alignment of the spectrometer, while the sigma corresponds to the sagitta resolution. The sagitta resolution is parametrized into two separate components: multiple scattering and intrinsic resolution, respectively dominating at high and low momenta. Using the solenoidal magnetic field of the Inner Detector to determine the momentum of the muon tracks, the intrinsic component of the sagitta resolution is isolated and found to be between 80 and 100 μm.

The hit residual distribution, track reconstruction efficiency and momentum resolution are studied using curved tracks collected with the solenoidal B-field at its nominal value, and are found to be very close to the design specifications for the MS. The hit residual is defined as

the distance between a reconstructed track and the position (drift radius) of its individual hits. The residual distribution for stand-alone tracks crossing three MDT chambers is found to be 104 μm, consistent with the measured sagitta resolution. The efficiency of track reconstruction is obtained by calculating the fraction of ID cosmic-ray tracks which are also reconstructed in the MS. The reconstruction efficiency for stand-alone tracks crossing two or more MDT chambers matches with the cosmic simulation, averaging 95% (see Fig. 1(b)).

To measure the momentum resolution of the MS without requiring a comparison with the ID, the top and bottom sections of a cosmic-ray track traversing the whole detector are compared. The momentum resolution is the width of the fitted distribution of relative p_T differences ($\Delta p_T/p_T$) between the top and bottom halves of the track. Fitting the momentum resolution against the momentum of the tracks (see Fig. 1(c)) allows the extraction of its three components: energy loss correction (P_0), multiple scattering (P_1), and intrinsic resolution (P_2). Extrapolating the fitted function to 1 TeV momenta gives a resolution of $11 \pm 2\%$ for tracks crossing small MDT chambers and $25 \pm 2\%$ for tracks crossing large ones. The difference between small and large chambers is due to the difference in integrated magnetic field along the muon paths. The design goal for 1 TeV muon tracks is a p_T resolution of approximately 10%.

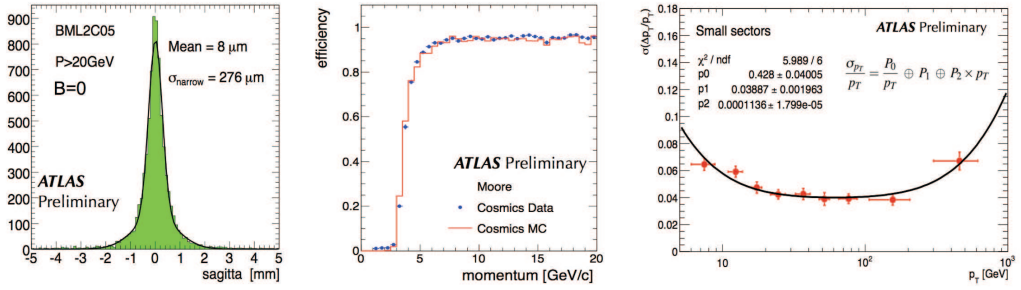

(a) (b) (c)

Figure 1: Performance results from a study of cosmic-ray tracks in the MS Barrel. A segment sagitta distribution (a), the reconstruction efficiency as a function of momentum for stand-alone tracks (b), and the p_T resolution as a function of p_T for small MDT sectors (c).

The second set of performance studies discussed here is for the most part based on the first 0.6 nb^{-1} of 7 TeV pp collisions triggered using the ATLAS Minimum Bias Trigger Scintillators. The hardware performance of the MS during these collision runs was good, with very low fractions of dead or noisy channels (0.3% for MDT, 1.5% for CSC, 2.7% for RPC, 1.2% for TGC), and the performance of the muon tracking chambers matches well our expectation from Monte-Carlo. Some basic distributions are shown, for both data and simulation, in figures 2(a) to 2(f). Here the Monte-Carlo is normalized to the number of events in the data. Using a larger dataset (6.4 nb^{-1}), the efficiency of the muon triggers relative to the tracking efficiency was measured by comparing triggered tracks with reconstructed tracks in the minimum-bias sample. The geometrical acceptance of the RPC trigger is around 80%, setting a limit for its relative efficiency, while the TGC efficiency reaches its plateau above 90% (see Figs. 2(g) and 2(h)).

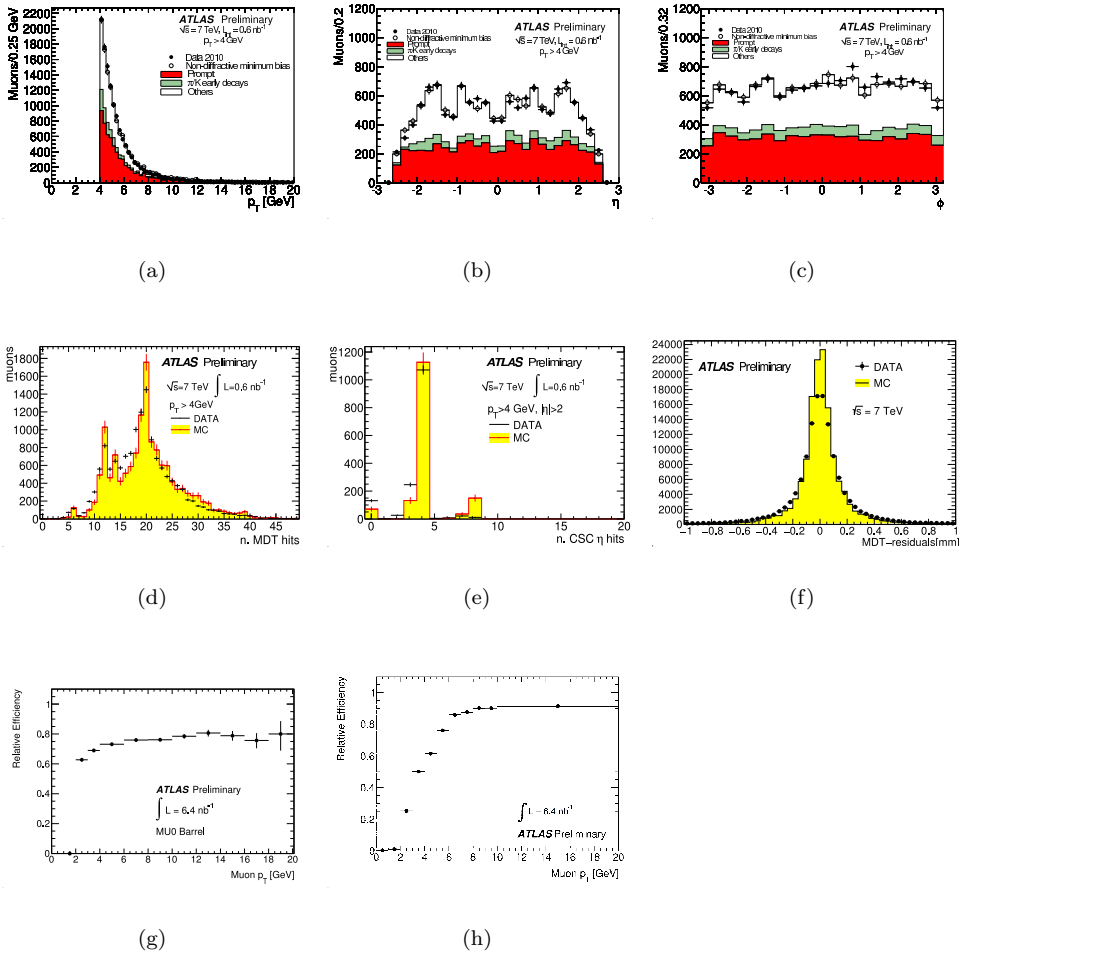

(a) (b) (c)

(d) (e) (f)

(g) (h)

Figure 2: Basic distributions obtained from collision muons compared to simulation: track p_T (a), η (b), and ϕ (c), number of MDT (d) and CSC (e) hits per combined track match the Monte-Carlo prediction well. The two peaks in (d) correspond to tracks crossing two and three chambers, respectively. The hit residual distribution (f) is slightly wider in data than in the simulation due to an underestimation of the material in the MS. (g) and (h): RPC and TGC trigger efficiencies for the lowest trigger threshold (MU0) relative to combined tracks.

References

[1] The ATLAS Collaboration, *Muon Performance in Minimum Bias pp Collision Data at* $\sqrt{s} = 7$ TeV *with ATLAS*. ATL-CONF-2010-036 (2010).

[2] The ATLAS Collaboration, *Preliminary studies for the measurement of the inclusive muon spectrum in pp collisions at* $\sqrt{s} = 7$ TeV *with the ATLAS detector*. ATL-CONF-2010-035 (2010).

[3] The ATLAS Collaboration, *First observation of the* $J/\psi \to \mu\mu$ *resonance in ATLAS pp collisions at* $\sqrt{s} = 7$ TeV. ATL-CONF-2010-045 (2010).

List of Authors

Alioli, Simone, 204
Amram, Nir, 358
Antola, Matti, 385
Artemenkov, Denis A., 400

Banfi, Andrea, 186
Bednyakov, Vadim A., 400
Benedetti, Daniele, 246
Biesiada, Jedrzej, 164
Blaizot, Jean-Paul, 373
Bonato, Alessio, 43
Brandt, Gerhard, 157
Broz, Michal, 219
Buras, Andrzej J., 325

Catà, Oscar, 311
Cerati, Giuseppe B., 214
Cogan, Julien, 354
Conti, Géraldine, 366
Cornelissen, Thijs, 67

Dainese, Andrea, 97
Demaria, Natale, 34
Dermíšek, Radovan, 279
DeViveiros, Pier-Olivier, 190

Espinosa, Jose R., 267

Feng, Eric, 241
Ferretto Parodi, Andrea, 412

Gallo, Elisabetta, 173
Gehrmann, Thomas, 134
Gelmini, Graciela B., 261
Gieseke, Stefan, 194
Gouzevitch, Maxime, 237
Grabowska-Bold, Iwona, 87
Graziano, Alberto, 271
Grojean, Christophe, 267
Guadagnoli, Diego, 295

Halyo, Valerie, 107
Heikinheimo, Matti, 385
Heinemeyer, Sven, 275, 291
Herrmann, Björn, 388
Heuer, Rolf-Dieter, 3
Hoepfner, Kerstin, 284
Höche, Stefan, 199

Isidori, Gino, 311

Jež, Pavel, 391
Jenni, Peter, 10

Kamenik, Jernej F., 311
Kant, Philipp, 394
Kerschen, Nicolas, 227
Khoze, Valery A., 275
Kniehl, Bernd A., 409, 418
Kono, Takanori, 299
Krasny, Mieczyslaw Witold, 250
Krauss, Frank, 199
Kreps, Michal, 317

Lamont, Mike, 15
Lee, Yen-Jie, 160
Lendermann, Victor, 288
Loddenkoetter, Thomas, 397
Lunardon, Marcello, 51
Lykasov, Gennady I., 400

Mühlleitner, Margarete, 267, 415
Maciuc, Florin, 39
Mackeprang, Rasmus, 91
Mager, Magnus, 55
Maire, Antonin, 168
Maniatis, Markos, 403
Mannel, Thomas, 342
Manteuffel, Andreas von, 403
Marco, Emanuele Di, 232
Meng, Zhaoxia, 406

Miśkowiec, Dariusz, 177
Mitsuka, Gaku, 29
Moortgat-Pick, Gudrid, 303

Nachtmann, Otto, 403

Palisoc, Caesar P., 409
Plätzer, Simon, 194
Potrap, Igor, 47
Pueschel, Elisa, 350

Röhr, Christian, 194
Radicci, Valeria, 59
Roland, Benoît, 223
Rolbiecki, Krzysztof, 303
Ryskin, Misha G., 275
Rzehak, Heidi, 415

Saleev, Vladimir, 418
Sannino, Francesco, 385
Santos, Helena, 379
Schöfbeck, Robert, 307
Schneider, Olivier, 119
Schukraft, Jürgen, 23
Schönherr, Marek, 199
Scodellaro, Luca, 71
Serrano, Justine, 362
Servant, Géraldine, 254
Seymour, Michael H., 147
Shipilova, Alexandera, 418
Siegert, Frank, 199
Siodmok, Andrzej, 194
Spira, Michael, 415

Tackmann, Kerstin, 63
Tasevsky, Marek, 275
Tattersall, Jamie, 303
Thom, Julia, 128
Torassa, Ezio, 181
Tuominen, Kimmo, 385

Volyanskyy, Dmytro, 421

Warsinsky, Markus, 209
Weiglein, Georg, 275
Wiedner, Dirk, 79
Wiglesworth, Craig, 424

Xíng, Fúnaì, 83

Yurkewicz, Adam, 75

Zenis, Tibor, 427
Zevi Della Porta, Giovanni, 430